Science Arts & Métiers (SAM)
is an open access repository that collects the work of Arts et Métiers Institute of Technology researchers and makes it freely available over the web where possible.

This is an author-deposited version published in: https://sam.ensam.eu
Handle ID: .http://hdl.handle.net/10985/22240

To cite this version :

Joseph PAUX, Léo MORIN, Renald BRENNER - A model of porous plastic single crystals based on fractal slip lines distribution - Journal of the Mechanics and Physics of Solids - Vol. 167, p.104948 - 2022

Any correspondence concerning this service should be sent to the repository Administrator : scienceouverte@ensam.eu

A model of porous plastic single crystals based on fractal slip lines distribution

Joseph Paux [a,*], Léo Morin [b], Renald Brenner [c]

[a] Institut de Thermique, Mécanique, Matériaux (ITheMM, EA 7548), Université de Reims Champagne-Ardenne, Campus Sup Ardenne, 08000 Charleville-Mézières, France
[b] PIMM, Arts et Metiers Institute of Technology, CNRS, Cnam, HESAM University, 151 boulevard de l'Hopital, 75013 Paris, France
[c] Sorbonne Université - CNRS, UMR 7190, Institut Jean Le Rond d'Alembert, 4 place Jussieu, 75005 Paris, France

A B S T R A C T

The ductile failure of crystalline materials is strongly linked to the growth of intragranular voids. The estimation of the overall yield criterion thus requires to take into account the anisotropic plastic behavior of the single crystal. In the framework of the kinematic limit-analysis approach, this problem has been considered up to now with Gurson-type isotropic trial velocity fields. In the present work, a different class of piecewise constant velocity fields is proposed based on a detailed analysis of FFT numerical results on the strain localization in porous single crystals with periodic distributions of voids. This original approach is implemented for the model 2D problem of a square or hexagonal array of cylindrical voids in a hexagonal close-packed single crystal with in-plane prismatic slip systems. For equibiaxial loadings, the assumption of discontinuous velocity field provides a good approximation of the smooth jumps observed in the numerical results. Consistently, this new proposal leads to a significant improvement on the macroscopic yield stress with respect to the estimate based on an isotropic velocity field. Our theoretical estimate almost coincides with the FFT numerical results for all the unit-cells and crystalline orientations considered.

1. Introduction

The mechanisms of void growth and coalescence are responsible for the ductile failure of crystalline materials, and occur by plastic flow around initial voids or nucleated cavities at second-phase particles. Those cavities can appear at two scales of a polycrystalline material, namely at the scale of grains (i.e. intragranular and intergranular porosities) and at the polycrystalline scale. Void growth will thus depend on the nature of the surrounding plastic behavior, which can be modeled by (i) crystal plasticity at the scale of grains and (ii) isotropic (or texture-induced anisotropic) plasticity at the polycrystal scale. Hence, the micromechanical modeling of void growth and coalescence requires to take into consideration those different local behaviors in order to account for the influence of the porosity on the macroscopic behavior. In general, it is not possible to derive analytical models for the plasticity of ductile porous solids. Two methods of homogenization have been proposed to estimate the plastic response of porous materials.

The first framework is based on Gurson (1977)'s pioneering work who has derived an approximate model for isotropic ductile porous solids by performing a kinematic limit-analysis of a hollow sphere subjected to conditions of homogeneous boundary strain rate. This model relies on the use of a trial velocity field, composed of the exact solution for the hydrostatic loading (Rice and Tracey, 1969) and a homogeneous velocity field for the deviatoric loading. Due to its intrinsic limitations (i.e. isotropic rigid-plastic

* Corresponding author.
E-mail address: joseph.paux@univ-reims.fr (J. Paux).

matrix and spherical cavity), this model has been extended in several directions. It has notably been extended to void shape effects which are important at low stress triaxiality, first with spheroidal voids (Gologanu et al., 1993) using (Lee and Mear, 1992)'s velocity fields, and later with ellipsoidal voids (Madou and Leblond, 2012a,b), using the incompressible velocity fields of Leblond and Gologanu (2008) satisfying conditions of homogeneous strain rate on every confocal ellipsoidal surfaces. The effect of hardening, which is important in cyclic ductile failure, has been considered by Leblond et al. (1995) and Morin et al. (2017) using sequential limit-analysis in which the local hardening evolves with Gurson (1977)'s trial velocity field. Finally, Gurson's model has also been extended to anisotropic materials, by considering a Hill-type yield criterion for the matrix (Benzerga and Besson, 2001), a single crystal plasticity model (Paux et al., 2015) or a strain gradient plasticity single crystal model (Khavasad and Keralavarma, 2021), using isotropic velocity fields.[1] The influence of local hardening in single crystals has been studied by Paux et al. (2018) through an estimation of the heterogeneity of the accumulated plastic strain, still relying on Gurson's isotropic velocity field. It is interesting to note that the above models have been derived using the (rudimentary) isotropic velocity field (Gurson, 1977) (and its subsequent extensions to ellipsoidal cavities) in the kinematic limit-analysis procedure. Other types of trial fields have been proposed to derive alternative models, such as the enriched Eshelby-like velocity fields of Monchiet et al. (2011) or the trial stress field of Cheng et al. (2014) using static limit-analysis.

The second framework is based on nonlinear homogenization, following the seminal work of Ponte Castañeda (1991) who proposed a variational homogenization approach which makes use of a linear comparison composite (LCC). Since then, it has been widely used and developed to tackle several micromechanical problems. This variational method was extended to the case of crystalline viscoplastic phases by deBotton and Ponte Castañeda (1995) who considered more general LCCs with anisotropic phases mimicking the symmetries of crystalline phases. An alternative extension was proposed by Idiart and Ponte Castañeda (2007) who considered the restrictive case of a two dimensional porous single crystal subjected to anti-plane strain loadings; this method produces tighter bounds than that of deBotton and Ponte Castañeda (1995) but it is generally considered harder to implement. The variational method of deBotton and Ponte Castañeda (1995), together with *ad hoc* modifications inspired from Gurson's model, has been used by Han et al. (2013) to derive the yield function of porous face-centered cubic (FCC) single crystals. This model was then extended to finite strains by Ling et al. (2016) by accounting for crystalline strain hardening laws as well as the evolution of the porosity. In addition, Mbiakop et al. (2015a) used a modification of the variational method of deBotton and Ponte Castañeda (1995) to derive the flow potentials of porous single crystals containing general ellipsoidal voids and subjected to general loadings (see also Mbiakop et al., 2015b). Finally, Song and Ponte Castañeda (2017) made use of the iterated approach of Agoras and Ponte Castañeda (2013), which leads to tighter bounds for porous single crystals.

Overall, those models provide good estimates of the macroscopic behavior of porous single crystals with moderate anisotropy such as in the case of FCC single crystals (Han et al., 2013; Paux et al., 2015; Mbiakop et al., 2015a), but are less accurate when anisotropy is more pronounced as it is the case for hexagonal close-packed (HCP) single crystals (Paux et al., 2018; Jossel et al., 2018). Furthermore, in the above models, the shape of the cavity considered is either spherical or ellipsoidal and the distribution of hardening is generally considered homogeneous or in spherical layers deduced from an isotropic growth of the cavity.

Nonetheless, numerical simulations of porous single crystals, either by the finite element method (FEM) or by the fast-Fourier transform (FFT method of Moulinec and Suquet (1998)), have shown that the strain and velocity fields in single crystals are highly anisotropic. Borg and Kysar (2007) have studied cylindrical voids embedded in a single crystal plasticity matrix (see also Subrahmanya Prasad et al., 2016) and they observed slip bands at the vicinity of the cavity.[2] Moreover, numerical FFT calculations performed by Paux et al. (2018) have shown that the distribution of the strain field in slip bands depends on the type of crystalline structure considered (FCC, HCP, etc.). Micromechanical cell calculations have shown that, during evolution, the cavity is not ellipsoidal, in general, and tends to a polyhedral shape at high stress triaxiality (Yerra et al., 2010; Srivastava and Needleman, 2013, 2015; Selvarajou et al., 2019). In addition, the plastic strain field becomes very heterogeneous during evolution and its distribution cannot be reproduced by isotropic velocity fields.

Experimental results on polycrystals with intragranular porosity have also shown that the cavities have faceted shapes. In the work of Crépin et al. (1996), the damage mechanisms of a β-treated zirconium HCP polycrystal are analyzed and it was observed that intragranular cavities are hexagonal with facets aligned with the slip directions. In addition, during the dynamic spallation of shock loaded pure aluminum FCC single crystal, it has been observed by X-ray tomography that voids have the shape of octahedrons (Hong et al., 2017). Finally, Barrioz et al. (2019) observed, in a solution annealed 304L austenitic stainless steel (which is used as a model FCC material), that dislocation channels strongly interact with voids at the irradiated state, emphasizing that the deformation mode is heterogeneous at the grain scale.

The accurate modeling of porous single crystals thus requires an anisotropic and heterogeneous description of the mechanical fields, notably the velocity field in order to reproduce accurately the voids shape as well as localized hardening in slip lines. A specific mention has to be made to the work of Gan and Kysar (2007) (see also Kysar et al., 2005; Gan et al., 2006) who derived analytically the solution for the plane strain stress field around a cylindrical void in a HCP single crystal: the stress field distribution is heterogeneous and defines a 'star' structure with self-similarity. However, the velocity field was not derived so this solution

[1] As explained in Morin et al. (2014), the reason isotropic velocity fields provide a good estimate of the yield surface even for anisotropic materials can be explained by the variational characterization of the overall yield locus in terms of the overall plastic dissipation. Indeed, if the anisotropy is *moderate*, the use of a trial isotropic velocity field (which slightly differs from the exact anisotropic one in the approximate limit-analysis) should lead to a reasonable estimate of the minimum of the plastic dissipation, leading itself to a good estimate of the yield locus.

[2] It must be noted that the distribution of slip bands can be modified when a *strain gradient* single crystal plasticity model is considered (Borg and Kysar, 2007).

does not permit to obtain a macroscopic yield criterion. Therefore, the aim of this work is to propose a new method for deriving velocity fields in porous single crystals which would allow the analytical calculation of the macroscopic plastic potential. The velocity field investigated is based on a fractal slip lines distribution mimicking the distribution of the strain field observed in numerical simulations of porous single crystals.

The paper is organized as follows. In Section 2, the distribution of the strain field in porous single crystals is investigated by FFT-based numerical limit-analysis. Based on these observations, theoretical trial velocity fields based on fractal slip lines distribution are derived in Section 3. In Section 4, the macroscopic yield criterion of porous single crystals is determined using fractal velocity fields. Finally, the results obtained are discussed in Section 5, by comparing the corresponding stress field with the solution of Gan and Kysar (2007), and by assessing the influence of the boundary conditions and the loading on the slip lines distribution.

2. FFT-based numerical limit-analysis of porous single crystals

2.1. Problem addressed

We consider a hexagonal close-packed single crystal containing cylindrical voids aligned with the sixfold symmetry axis ($\mathbf{c}$-axis) and periodically distributed on hexagonal or square arrays. A rate-independent elastoplastic constitutive law is assumed with plastic deformation occurring by dislocation glide on slip systems. A slip system k is characterized by the unit normal to the slip plane $\mathbf{n}_k$ and the unit slip direction $\mathbf{m}_k$ which define the Schmid tensor $\boldsymbol{\mu}_k = 0.5\,(\mathbf{n}_k \otimes \mathbf{m}_k + \mathbf{m}_k \otimes \mathbf{n}_k)$. The present study is restricted to plane strain conditions with three in-plane prismatic slip systems oriented at $\pi/3$ (Fig. 1).

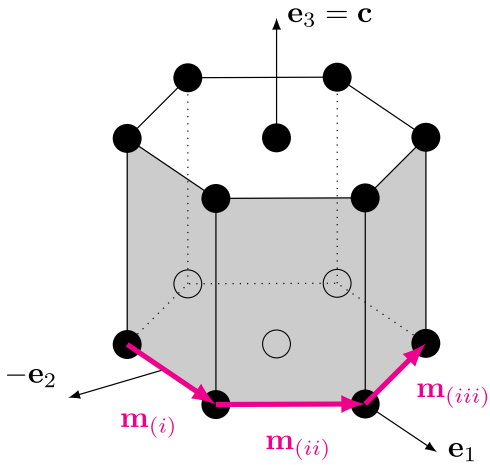

Fig. 1. Hexagonal Bravais lattice and prismatic slip systems.

According to the Schmid law, a slip system k can be activated if the absolute value of the resolved shear stress $\tau_k = \boldsymbol{\sigma} : \boldsymbol{\mu}_k$ reaches a critical value τ_k^c. Consequently, the yield function of the single crystal is defined by a multi-criterion which reads

$$f(\boldsymbol{\sigma}) = \sup_{k=1,\dots,3} |\boldsymbol{\sigma} : \boldsymbol{\mu}_k| - \tau_k^c = \sup_{k=1,\dots,3} f_k(\boldsymbol{\sigma}) \quad \text{with} \quad f(\boldsymbol{\sigma}) \leq 0. \tag{1}$$

From the generalized normality rule, the plastic strain rate corresponding to the Schmid criterion is given by

$$\dot{\boldsymbol{\varepsilon}}^p = \sum_{k=1}^{3} \dot{\gamma}_k \frac{\partial f_k}{\partial \boldsymbol{\sigma}} = \sum_{k=1}^{3} \dot{\gamma}_k\, \boldsymbol{\mu}_k\, \mathrm{sgn}(\tau_k) \quad \text{with} \quad \dot{\gamma}_k \geq 0,\ \dot{\gamma}_k f_k(\boldsymbol{\sigma}) = 0,\ \forall k \in [1;3]. \tag{2}$$

$\dot{\gamma}_k(\mathbf{x})$ is the plastic slip rate on slip system k. In the present study, since we consider a single slip systems family, we have $\tau_k^c = \tau_c$, $\forall k$.

Two different crystalline orientations are considered with $\theta = 0°$ and $15°$, where θ is the angle between the slip direction of the first system ($\mathbf{m}_{(i)}$) and the unit vector $\boldsymbol{e}_1$ (see Fig. 2b and d). We thus study four microstructures which result from the combination of a unit-cell and a crystalline orientation, denoted by H0 (hexagonal with aligned crystal orientation $\theta = 0°$), H15 (hexagonal unit-cell with rotated crystal orientation $\theta = 15°$), S0 (square unit-cell with aligned crystal orientation $\theta = 0°$) and S15 (square unit-cell with rotated crystal orientation $\theta = 15°$). They are represented schematically in Fig. 2. For hexagonal unit-cells, the apothem is denoted by h and the void radius by ρ, so that the porosity (volume fraction of void) reads $f = \pi(\rho/h)^2/(2\sqrt{3})$. For square unit-cells, the side is denoted by a and the void radius by ρ, so that the porosity reads $f = \pi(\rho/a)^2$.

In the sequel, the macroscopic stress as well as the local velocity fields will be investigated in the sole case of a hydrostatic loading.

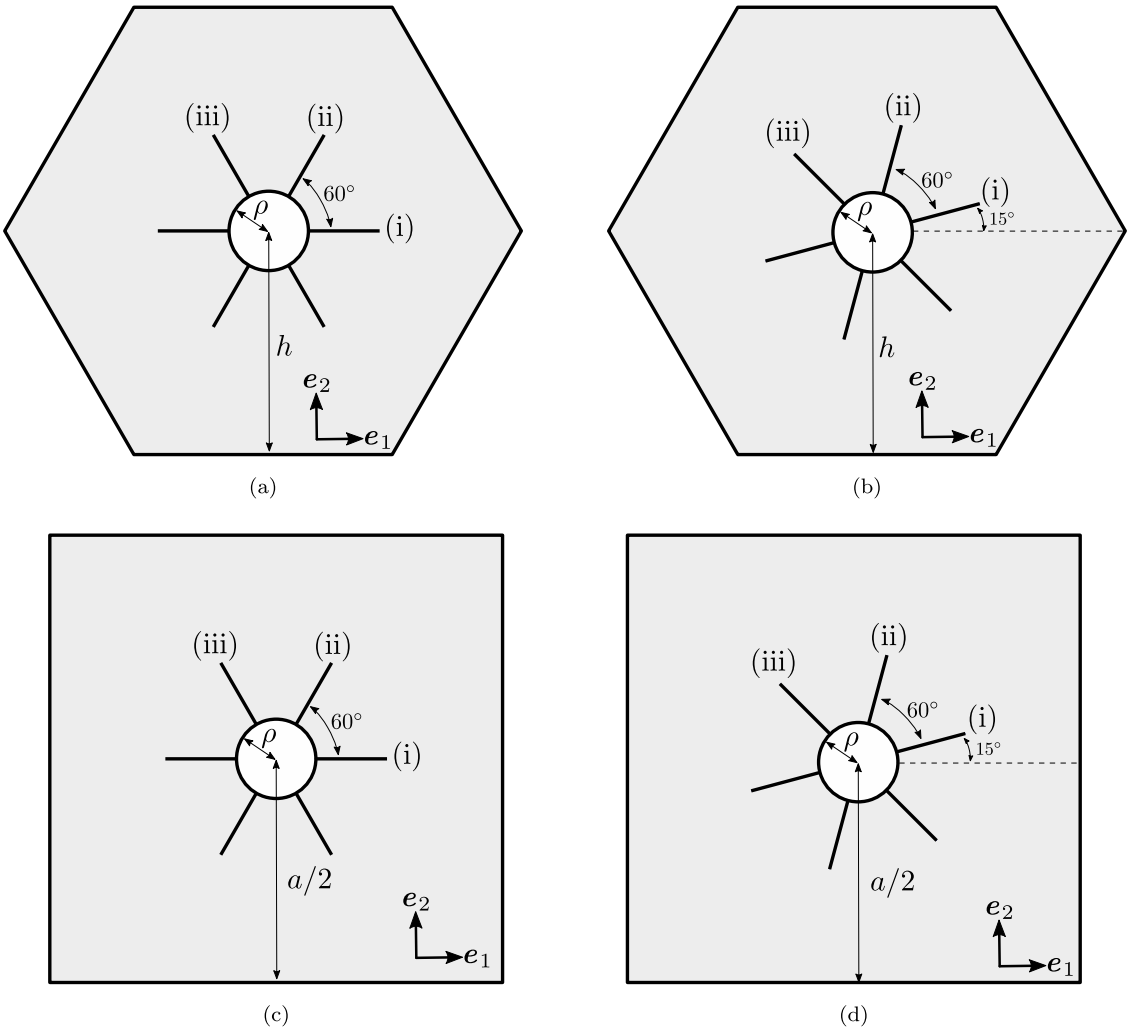

Fig. 2. Studied microstructures: (a) Hexagonal unit-cell with aligned crystal orientation $\theta = 0°$ (H0), (b) Hexagonal unit-cell with rotated crystal orientation $\theta = 15°$ (H15), (c) Square unit-cell with aligned crystal orientation $\theta = 0°$ (S0), (d) Square unit-cell with rotated crystal orientation $\theta = 15°$ (S15).

2.2. Simulation framework

The set of equations of the local problem to be solved on a unit-cell Ω with boundary $\partial\Omega$ reads

$$\begin{cases} \boldsymbol{\varepsilon}(\mathbf{x},t) &= \frac{1}{2}(\boldsymbol{\nabla}\mathbf{u}(\mathbf{x},t) + \boldsymbol{\nabla}\mathbf{u}^{\mathrm{T}}(\mathbf{x},t)), & \forall(\mathbf{x},t) \in \Omega \times [0;T] \\ \dot{\boldsymbol{\sigma}}(\mathbf{x},t) &= \mathbf{C}(\mathbf{x}) : (\dot{\boldsymbol{\varepsilon}}(\mathbf{x},t) - \dot{\boldsymbol{\varepsilon}}^p(\mathbf{x},t)), \quad \operatorname{div}\boldsymbol{\sigma}(\mathbf{x},t) = \mathbf{0}, & \forall(\mathbf{x},t) \in \Omega \times [0;T] \\ \mathbf{u}(\mathbf{x},t) &= \mathbf{E}(t).\mathbf{x} + \mathbf{u}'(\mathbf{x},t), \ \mathbf{u}' \text{ periodic on } \partial\Omega, & \forall t \in [0;T]. \end{cases} \tag{3}$$

with $\mathbf{E}(t)$, $t \in [0;T]$, a prescribed macroscopic strain. The tensor of elastic moduli $\mathbf{C}(\mathbf{x})$ is uniform in the single crystal ($\mathbf{C}(\mathbf{x}) = \mathbf{C}_{sc}$) and vanishes inside the void. The macroscopic strain and stress, denoted by $\mathbf{E}$ and $\boldsymbol{\Sigma}$, are classically defined as the volume averages of their microscopic counterparts $\boldsymbol{\varepsilon}$ and $\boldsymbol{\sigma}$:

$$\mathbf{E} = \langle \boldsymbol{\varepsilon} \rangle_\Omega, \quad \boldsymbol{\Sigma} = \langle \boldsymbol{\sigma} \rangle_\Omega, \tag{4}$$

where $\langle \cdot \rangle_\Omega$ denotes the spatial average over the representative cell Ω:

$$\langle f \rangle_\Omega = \frac{1}{\mathrm{vol}(\Omega)} \int_\Omega f \, \mathrm{d}\Omega. \tag{5}$$

The heterogeneous elastoplastic problem is classically solved by discretizing the time interval $[0;T]$. The stress and strain fields at each time t_i are determined by using a FFT-based numerical scheme for a composite material with a nonlinear local constitutive

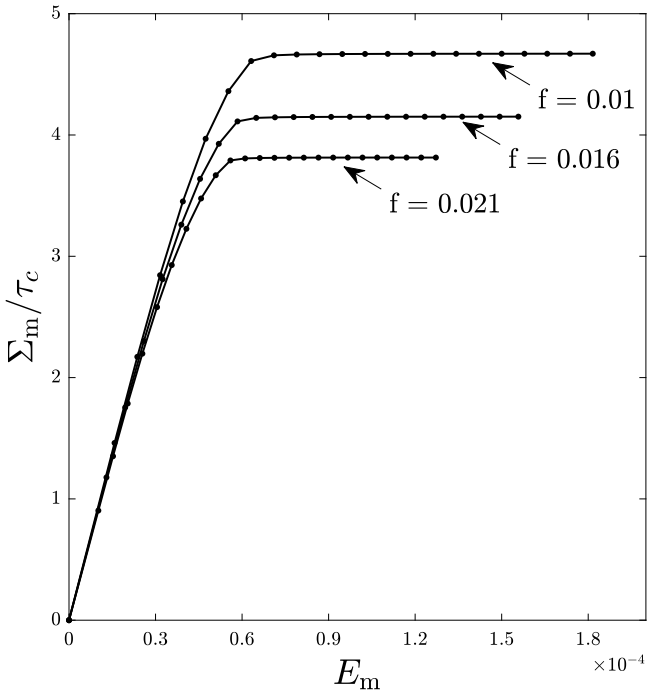

Fig. 3. Macroscopic responses obtained with the FFT numerical scheme for the square unit-cell with aligned crystal orientation $\theta = 0°$ (S0) and different porosities f.

law. For more details on the FFT numerical method, widely used in micromechanics for composites and polycrystalline materials, the reader is referred to Moulinec and Suquet (1998) and Michel et al. (2001). Its implementation for a rate-independent plastic porous crystalline material is detailed in Paux et al. (2018). For the hexagonal cells, the domain considered is a rectangle discretized using 3142 × 1814 pixels and for the square cells, the domain considered is a square discretized using 3000 × 3000 pixels (see Fig. 8 for an illustration of the discretization).

Illustrative results of the macroscopic response for an equibiaxial stress loading are shown in Fig. 3, where the macroscopic mean stress and strain are respectively defined as $\Sigma_m = \mathrm{Tr}(\boldsymbol{\Sigma})/2$ and $E_m = \mathrm{Tr}(\mathbf{E})/2$. The plateau corresponds to the yield stress of the porous single crystal.

2.3. Strain field and fractal slip line networks

Representative distributions of the equivalent von Mises strain in the H0, H15, S0 and S15 cells are given in Figs. 4, 5, 6 and 7, respectively. An illustration of the induced velocity field is given in Fig. 8. For all the FFT computations performed, the strain is mainly concentrated in lines, either parallel to a slip direction $\mathbf{m}_k$ (classical slip band) or a slip plane normal $\mathbf{n}_k$ (kink band). Thus, we propose to approximate and model the strain fields observed numerically as a *slip line network*. For each of the cells, comparison for different porosities suggests that the slip line networks are mainly made of a pattern recursively repeated with self-similarity from the exterior of the cell up to the void. Those patterns can be extended for any lower porosity by repeating them indefinitely to the cell centers. The induced infinite patterns then form fractal slip line networks.

For the H15 and S15 cells, the slip line networks are mainly constituted of a pattern of twenty four slip lines represented in blue in Figs. 9(b) and 10(b). This pattern is recursively repeated up to the void, forming successive layers, with homotheties of $\sqrt{3}/3$ from one layer to the following one. The S0 cell is made of the same pattern with a rotation of 15°, as shown in Fig. 10(a).

Besides, the H0 cell has a different fractal structure, with a repeated pattern made of two successive layers of twelve slip lines represented in blue in Fig. 9(a). Each of these two layers can be seen as the general pattern of twenty four slip lines observed for the S0 cell, but missing half the lines. Then, this twenty four slip lines pattern is the constitutive pattern of all the observed slip line networks and seems to be an inherent structure of the strain field in the considered porous single crystal.

For all the cells, the slip line network crosses the cell boundary at the middles of the boundary edges. For the H15, S0 and S15 cells, the fractal pattern changes in the exterior of the cell: an adaptative network of slip lines, represented in red in Figs. 9(b), 10(a) and 10(b), links the fractal to the boundary of the cell. Again, the adaptative layers can be seen as the general twenty four lines layer with missing and/or truncated lines.

Each slip line orientation of the slip line network can be identified to a slip plane normal or a slip direction. Then, an exact reconstruction of the slip line network has been performed through geometrical considerations and recursive deductions enabled by the fractal features described above. The results are displayed in Figs. 9(a) (H0), 9(b) (H15), 10(a) (S0) and 10(b) (S15).

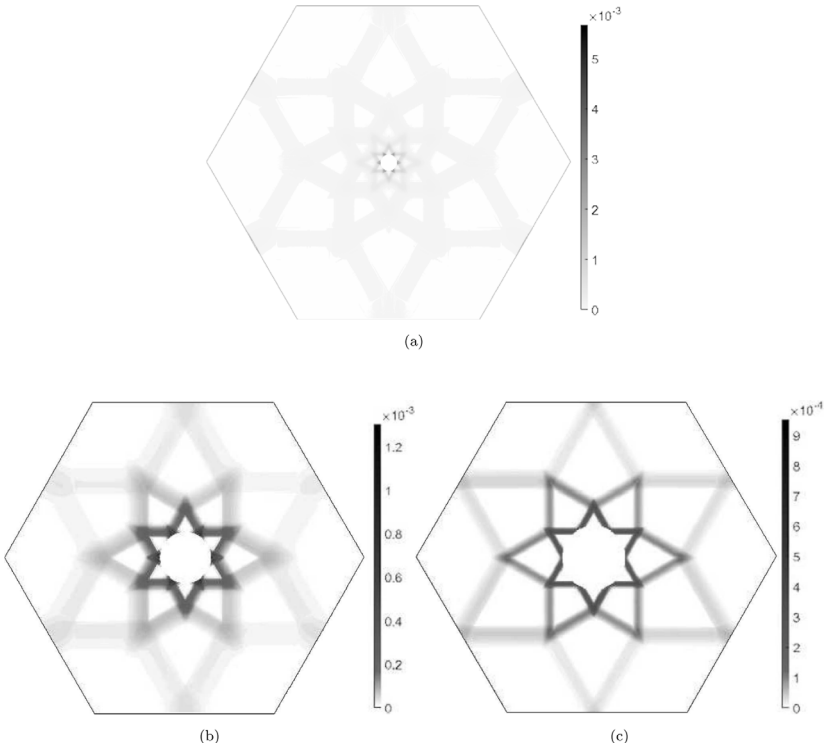

Fig. 4. Equivalent von Mises strain in the H0 cell for (a) $f = 0.24\%$, (b) $f = 2.42\%$ and (c) $f = 4\%$.

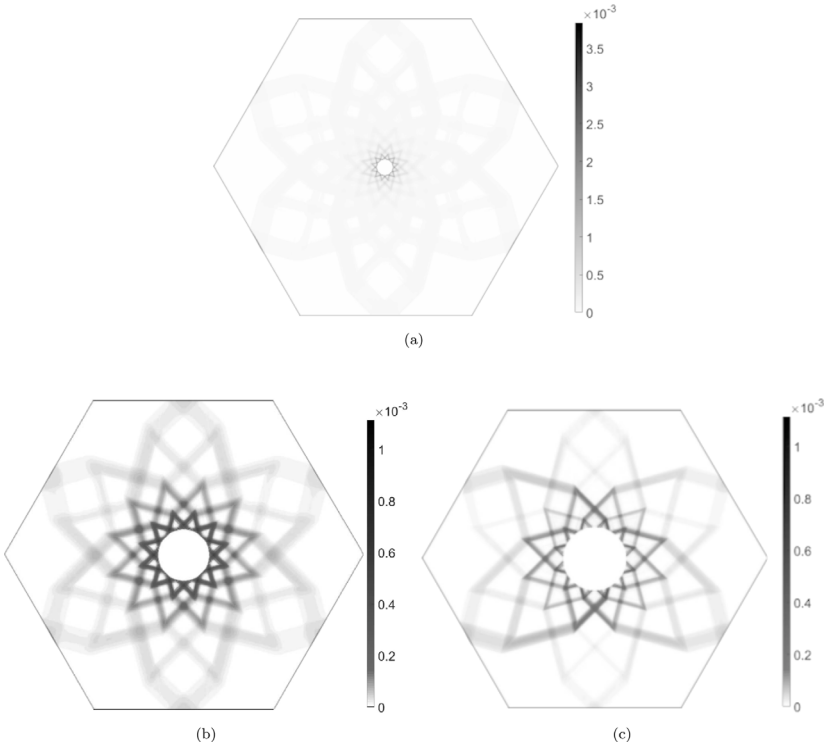

Fig. 5. Equivalent von Mises strain in the H15 cell for (a) $f = 0.24\%$, (b) $f = 2.42\%$ and (c) $f = 4\%$.

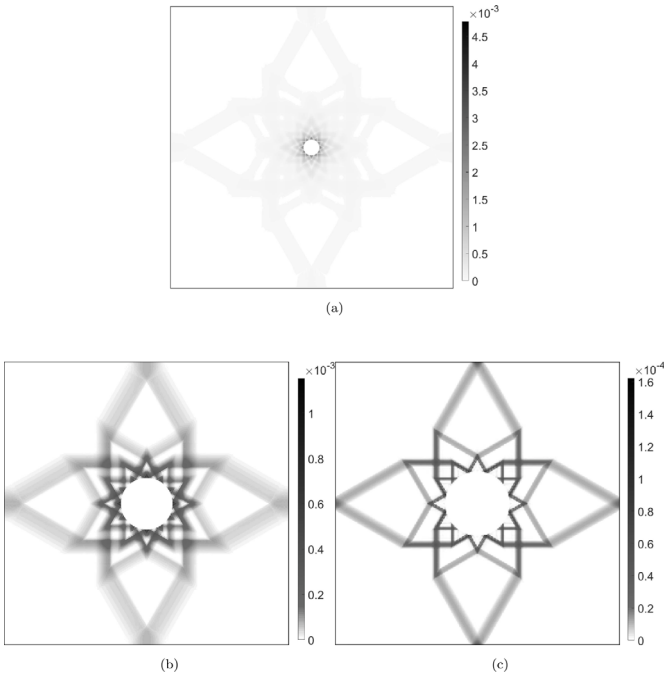

Fig. 6. Equivalent von Mises strain in the S0 cell for (a) $f = 0.24\%$, (b) $f = 2.42\%$ and (c) $f = 4\%$.

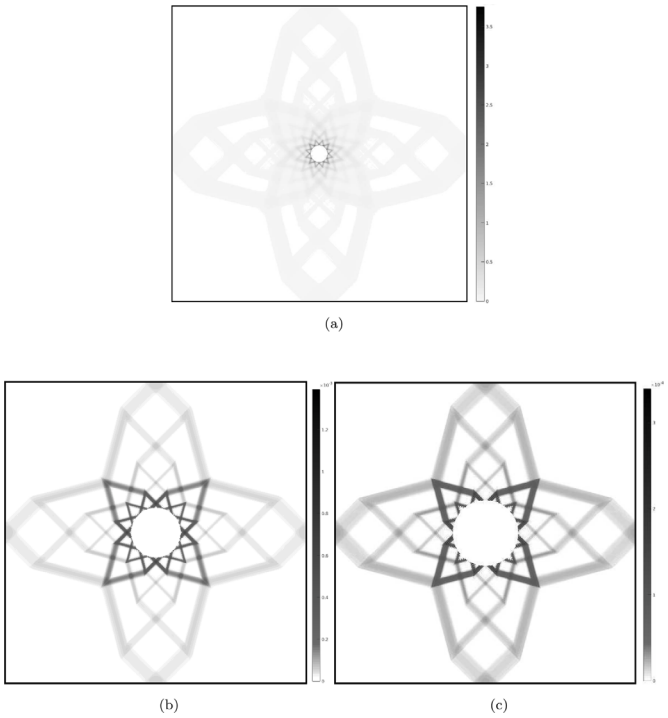

Fig. 7. Equivalent von Mises strain in the S15 cell for (a) $f = 0.24\%$, (b) $f = 2.42\%$ and (c) $f = 4\%$.

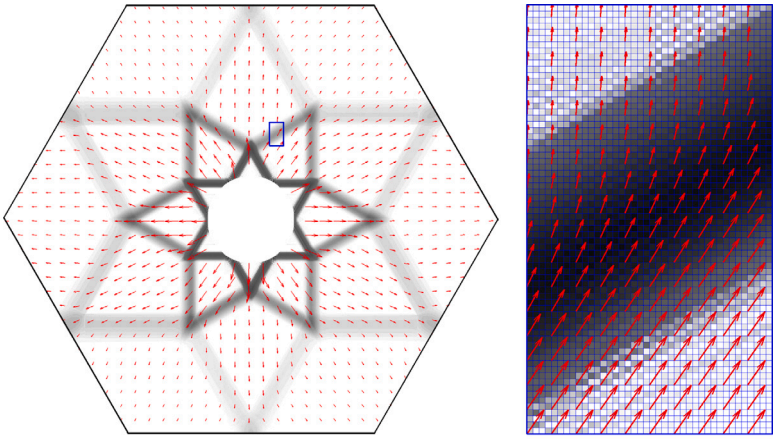

(a) (b)

Fig. 8. Illustration of (a) the velocity field in the H0 cell and (b) the discretization in the box indicated in blue in (a).

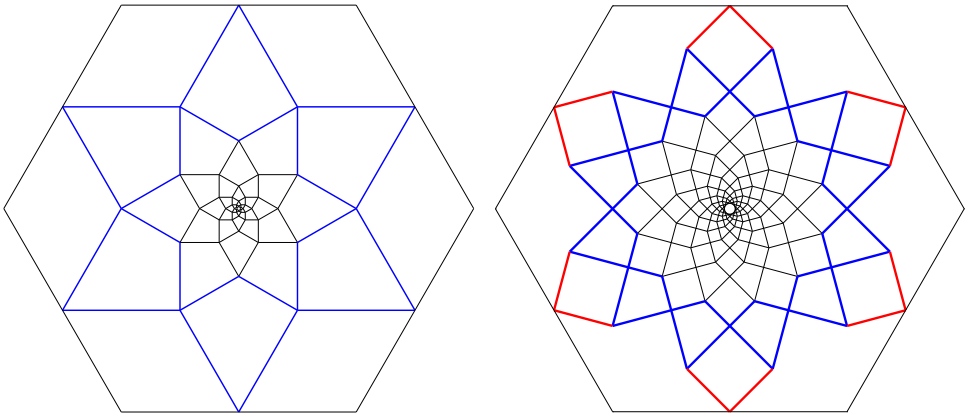

(a) (b)

Fig. 9. Slip line fractal networks for the hexagonal cells. (a) H0 cell and (b) H15 cell.

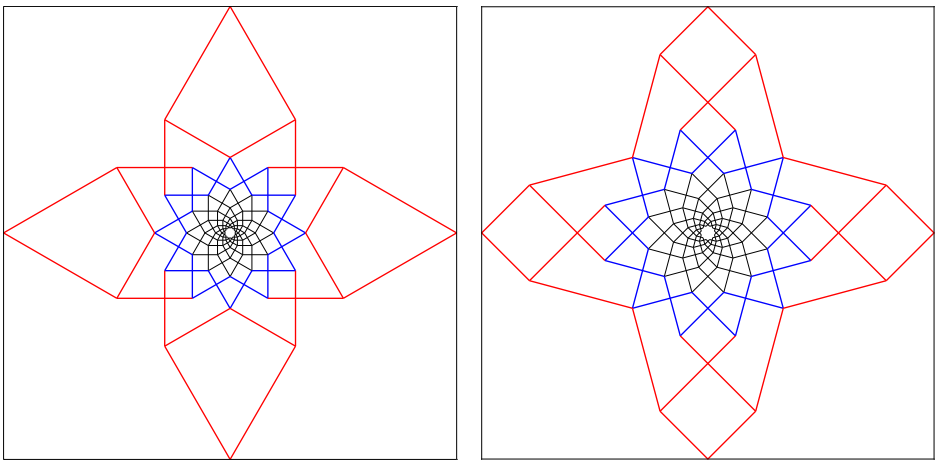

(a) (b)

Fig. 10. Slip line fractal networks for the square cells. (a) S0 cell and (b) S15 cell.

3. Theoretical trial velocity fields based on fractal slip lines distribution

3.1. Slip line based velocity field and node condition

In order to derive a trial velocity field from the slip line networks obtained in Section 2.3, we have chosen to consider the set of piecewise constant velocity fields. The plastic strain rate (2) being incompressible ($\mathrm{tr}\left(\boldsymbol{\mu}_k\right) = 0, \forall k$), the admissibility of the velocity field implies that the difference between the velocities of two adjacent blocks is co-linear to the slip line separating the blocks. Then, considering two blocks separated by a classical slip band, i.e a slip line along a slip direction $\mathbf{m}$ and orthogonal to a slip plane normal $\mathbf{n}$ as in Fig. 11, the velocities $\mathbf{v}_1$ and $\mathbf{v}_2$ of block 1 and 2 verify

$$(\mathbf{v}_2 - \mathbf{v}_1).\mathbf{n} = \mathbf{0}. \tag{6}$$

To characterize the intensity of the slip between the blocks, we introduce the algebraic slip line velocity $\dot{\Gamma}$ such that

$$\mathbf{v}_2 - \mathbf{v}_1 = \dot{\Gamma}\mathbf{m}. \tag{7}$$

Given the crystalline nature of a slip line, $\dot{\Gamma}$ is equivalent to a slip rate $\dot{\gamma}$ (see Eq. (2)) concentrated in the slip line, i.e a Dirac distribution $\dot{\gamma}\delta$. In addition, this description of the velocity field is also adapted for the kink bands by switching the slip plane normal $\mathbf{n}$ and the slip direction $\mathbf{m}$ in Eqs. (6) and (7). In the following, the sign convention for the slip line velocity $\dot{\Gamma}$ is represented by two half arrows as in Fig. 11. Given a slip line velocity $\dot{\Gamma}$, the velocity $\mathbf{v}_1$ of block 1 (resp. $\mathbf{v}_2$) is given by the velocity $\mathbf{v}_2$ (resp. $\mathbf{v}_1$) plus $\dot{\Gamma}$ times the vector indicated by the half arrow in the block 1 (resp. in the block 2). Following this convention, the relation between $\mathbf{v}_1$ and $\mathbf{v}_2$ as represented in Fig. 11 reads

$$\mathbf{v}_1 = \mathbf{v}_2 + \dot{\Gamma}(-\mathbf{m}) \quad ; \quad \mathbf{v}_2 = \mathbf{v}_1 + \dot{\Gamma}\mathbf{m}. \tag{8}$$

Then, the velocity field is entirely defined by the boundary conditions and the slip line velocities of all the slip line networks. Indeed, one can deduce the velocities in all the blocks from the velocity of one block and by passing from block to block using relation (8). As the strain is entirely concentrated in the slip lines, we will focus solely on the determination of the slip line velocities $\dot{\Gamma}$.

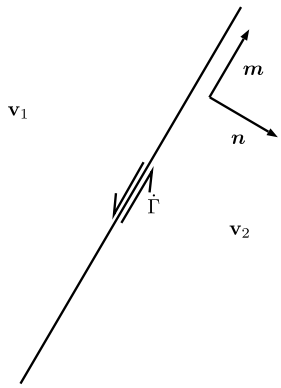

Fig. 11. Representation convention for the slip line velocity.

To be consistent, the slip line velocities must generate a coherent velocity field. Indeed, given a block 1 with a known velocity $\mathbf{v}_1$, the velocity $\mathbf{v}_2$ of a distant block 2 is obtained by considering a path from block 1 to block 2 and using relation (8) at each crossed slip line. If the slip line velocities are consistent, the obtained velocity $\mathbf{v}_2$ does not rely on the chosen path. On the example proposed in Fig. 12, the two given paths give respectively

$$\mathbf{v}_2 = \mathbf{v}_1 - \dot{\Gamma}_1\mathbf{m}_1 - \dot{\Gamma}_2\mathbf{m}_2, \tag{9}$$

$$\mathbf{v}_2 = \mathbf{v}_1 + \dot{\Gamma}_4\mathbf{m}_4 + \dot{\Gamma}_3\mathbf{m}_3. \tag{10}$$

Then, Eqs. (9) and (10) provide the following condition on the slip line velocities:

$$\dot{\Gamma}_1\mathbf{m}_1 + \dot{\Gamma}_2\mathbf{m}_2 + \dot{\Gamma}_4\mathbf{m}_4 + \dot{\Gamma}_3\mathbf{m}_3 = \mathbf{0}. \tag{11}$$

The condition given by Eq. (11) must be verified for every possible path between two blocks of the slip line network. Fortunately, one can demonstrate that the induced set of equations reduces to the equations given by the paths rounding the nodes of the slip line network as displayed in blue in Fig. 12. These paths lead to

$$\dot{\Gamma}_1\mathbf{m}_1 + \dot{\Gamma}_4\mathbf{m}_4 + \dot{\Gamma}_5\mathbf{m}_5 = \mathbf{0}, \tag{12}$$

$$-\dot{\Gamma}_2\mathbf{m}_2 - \dot{\Gamma}_3\mathbf{m}_3 + \dot{\Gamma}_5\mathbf{m}_5 = \mathbf{0}. \tag{13}$$

The combination of (12) in (13) permits to retrieve Eq. (11). Then, the field is consistent if and only if the condition (12) is verified for all nodes in the slip line network. In the following, it is named the *node condition*. In the general case, the determination of the slip line velocities is done in two steps:

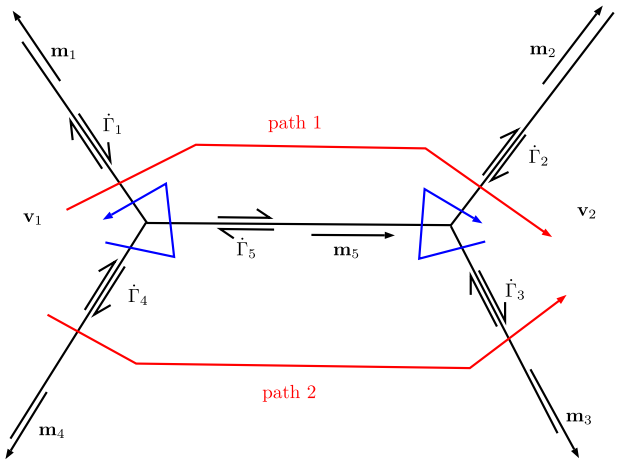

Fig. 12. Example of a slip line network with given slip line velocities. The red arrows give two different paths linking block 1 to block 2 by crossing different slip lines. The blue arrows represent the paths rounding the nodes of the slip line network.

1. Express the boundary conditions and deduce the slip line velocities in contact with the boundary of the cell.
2. Express the node condition at each node of the slip line network and deduce the slip line velocities in the entire cell.

In the following, we apply this method to the fractal networks obtained in Section 2.3. Looking closely to the fractal networks (Figs. 9 and 10), one can remark that all the four slip lines nodes have the same configuration (with rotations of 15°). This configuration is recalled in Fig. 13. Moreover, the three slip lines nodes can be seen as the same type of node with a fictitious zero velocity fourth slip line. The node condition can thus be expressed for this case and reused for all the nodes of the fractal networks. For the nodes considered, the slip lines 1 and 2 are always outward the fractal network while the slip lines 3 and 4 are towards the fractal network. Then, one needs to express the slip velocities $\dot{\Gamma}_3$ and $\dot{\Gamma}_4$ in function of $\dot{\Gamma}_1$ and $\dot{\Gamma}_2$. The node condition reads

$$\dot{\Gamma}_1\mathbf{m}_1 + \dot{\Gamma}_2\mathbf{m}_2 + \dot{\Gamma}_3\mathbf{m}_3 + \dot{\Gamma}_4\mathbf{m}_4 = \mathbf{0} \tag{14}$$

which leads to

$$\dot{\Gamma}_3 = \frac{2\sqrt{3}}{3}\dot{\Gamma}_1 - \frac{\sqrt{3}}{3}\dot{\Gamma}_2, \tag{15}$$

$$\dot{\Gamma}_4 = -\frac{\sqrt{3}}{3}\dot{\Gamma}_1 + \frac{2\sqrt{3}}{3}\dot{\Gamma}_2. \tag{16}$$

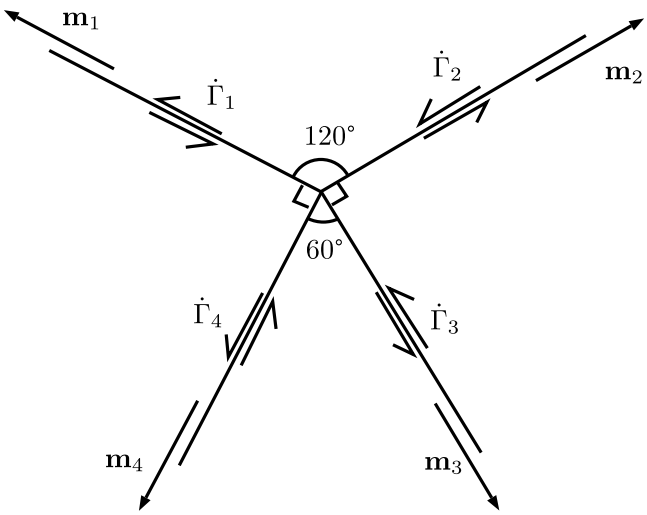

Fig. 13. Four slip lines node.

3.2. Velocity field for the H0 cell

In this section, the method presented in Section 3.1 is deployed to determine the velocity field of the H0 cell. Similar developments for the H15, S0 and S15 cells are given in Appendices A.1–A.3, respectively.

Conventions (slip line velocities and block names) are given in Fig. 14. We name layer i the ith group of slip lines from the boundary of the cell. For example, the set of slip lines in contact with the boundary is layer zero, the set of slip lines in contact with layer zero is layer one, and so on.

Due to the symmetries of the cell, the slip line velocities of a given layer are all equal. We note $\dot{\Gamma}_i$ the slip line velocity in layer i. For a better understanding, $\dot{\Gamma}_0$ and $\dot{\Gamma}_1$ are represented in Fig. 14. Besides, the symmetries give the velocities' directions in the blocks A_j and B_j. They read

$$\mathbf{v}_{A_j} = v_A \left(\cos \frac{j\pi}{3} \mathbf{e}_1 + \sin \frac{j\pi}{3} \mathbf{e}_2 \right), \tag{17}$$

$$\mathbf{v}_{B_j} = v_B \left(\cos \left[\frac{\pi}{6} + \frac{j\pi}{3} \right] \mathbf{e}_1 + \sin \left[\frac{\pi}{6} + \frac{j\pi}{3} \right] \mathbf{e}_2 \right). \tag{18}$$

First, one uses the boundary conditions to determine the velocities in the external layer. Using the Green theorem, the mean strain condition provides

$$\mathbf{D} = D_m \mathbf{I} = \frac{1}{\mathrm{vol}(\Omega)} \int_\Omega \mathbf{d}\, \mathrm{d}\Omega = \frac{1}{\mathrm{vol}(\Omega)} \int_S \frac{1}{2} (\mathbf{v} \otimes \mathbf{n} + \mathbf{n} \otimes \mathbf{v}) \mathrm{d}S, \tag{19}$$

where $\mathbf{D}$ is the macroscopic strain rate, $\mathbf{d}$ is its microscopic counterpart and $\mathbf{n}$ is the normal vector of the boundary of the cell. The trace of (19) gives

$$2D_m = \frac{1}{\mathrm{vol}(\Omega)} \int_S (v_1 n_1 + v_2 n_2) \mathrm{d}S = \frac{1}{\mathrm{vol}(\Omega)} \int_S \mathbf{v}.\mathbf{n}\, \mathrm{d}S. \tag{20}$$

The scalar product $\mathbf{v}.\mathbf{n}$ is constant over the boundary and equal to $v_A \cos(\pi/6)$. This implies that

$$v_A = \frac{2\sqrt{3}}{3} D_m h. \tag{21}$$

Applying relation (6) for the slip line between block A_0 and block B_0,

$$(\mathbf{v}_{A_0} - \mathbf{v}_{B_0}).\mathbf{n} = 0, \tag{22}$$

we obtain $v_B = \sqrt{3}\, v_A$. Finally, we deduce the slip line velocity $\dot{\Gamma}_0$ through the slip line condition (7) reading

$$\dot{\Gamma}_0 \mathbf{m} = \mathbf{v}_{A_0} - \mathbf{v}_{B_0}, \tag{23}$$

leading to

$$\dot{\Gamma}_0 = \left\| \mathbf{v}_{A_0} - \mathbf{v}_{B_0} \right\| = \frac{2\sqrt{3}}{3} D_m h. \tag{24}$$

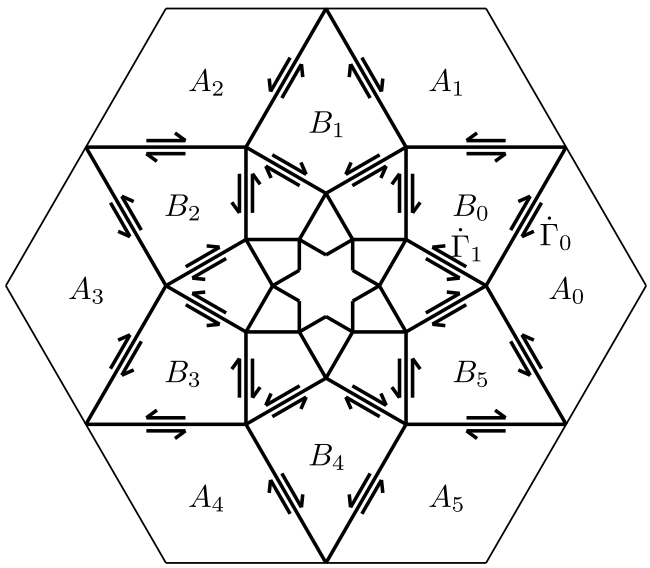

Fig. 14. Conventions for the determination of the H0 cell velocity field.

At this point, the boundary conditions led to the slip line velocities of the external layer of the fractal network. Then, we use the node condition to determine recursively the slip line velocities of the internal layers. The node condition (15) of any node between layers i and $i+1$ reads

$$\dot{\Gamma}_{i+1} = \frac{\sqrt{3}}{3}\dot{\Gamma}_i - \frac{2\sqrt{3}}{3}(-\dot{\Gamma}_i) = \sqrt{3}\,\dot{\Gamma}_i. \tag{25}$$

Using Eqs. (24) and (25), it follows that the slip line velocity in the layer i is given by

$$\dot{\Gamma}_i = \dot{\Gamma}_0\sqrt{3}^i = \frac{2\sqrt{3}^{i+1}}{3}D_m h. \tag{26}$$

3.3. Comparison with the numerical velocity field

For each cell (H0, H15, S0 and S15), the obtained velocity fields, deduced from the slip line velocities, the external velocities $\mathbf{v}_{A_j}$ and relation (7) are assessed by comparison with the numerical FFT velocity fields. The results are also compared with the isotropic velocity field derived by Gurson (1977) (see also Rice and Tracey, 1969) for a cylindrical cell with corresponding void radius and porosity. The magnitude of the velocity is represented along lines from the center of the cells. A typical result for a high porosity ($f = 4\%$) is given in Fig. 15 for the S0 cell (along a horizontal line and a 45° line). Overall, a very good agreement is observed between the numerical velocity field and the theoretical one. The theoretical velocity fields are piecewise functions with jumps at the slip line crossing, while the numerical velocity field appears to have a similar structure, but with smooth jumps between the blocks. The widths of the smoothed jumps correspond to the widths of the numerical slip lines (see Fig. 6c). The velocity in the blocks and the magnitude of the jump, corresponding to the slip line velocity, are well reproduced. Besides, comparison of the velocity along two different lines highlights the anisotropy of the velocity field (Fig. 15). The isotropic velocity lies between the two lines of the anisotropic velocity field and can then be considered as a good approximation of the velocity field.

The same comparisons are presented for a lower porosity ($f = 0.24\%$) in Figs. 16 and 17, respectively for the hexagonal and square cells. Again, the velocities in the blocks are well reproduced, justifying the hypotheses used to determine the slip line velocities. In some cases, the jump between the blocks is hardly visible for the numerical velocity fields. Indeed, as can be seen in Fig. 4(a), 5(a), 6(a) and 7(a), the band widths are more important for this porosity and there is strain in the blocks of the deep layers of the slip line network. Still, the anisotropy of the velocity field is well reproduced by the theoretical velocity field proposed.

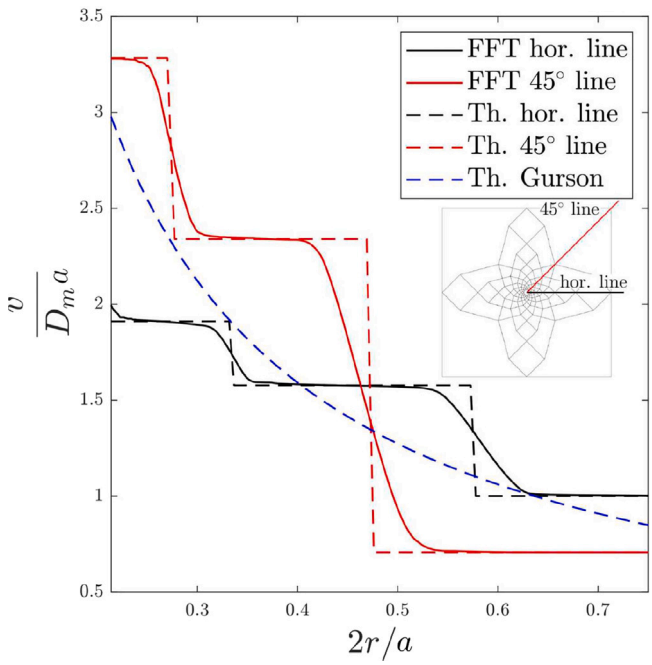

Fig. 15. Velocity along lines of the S15 cell with $f = 4\%$.

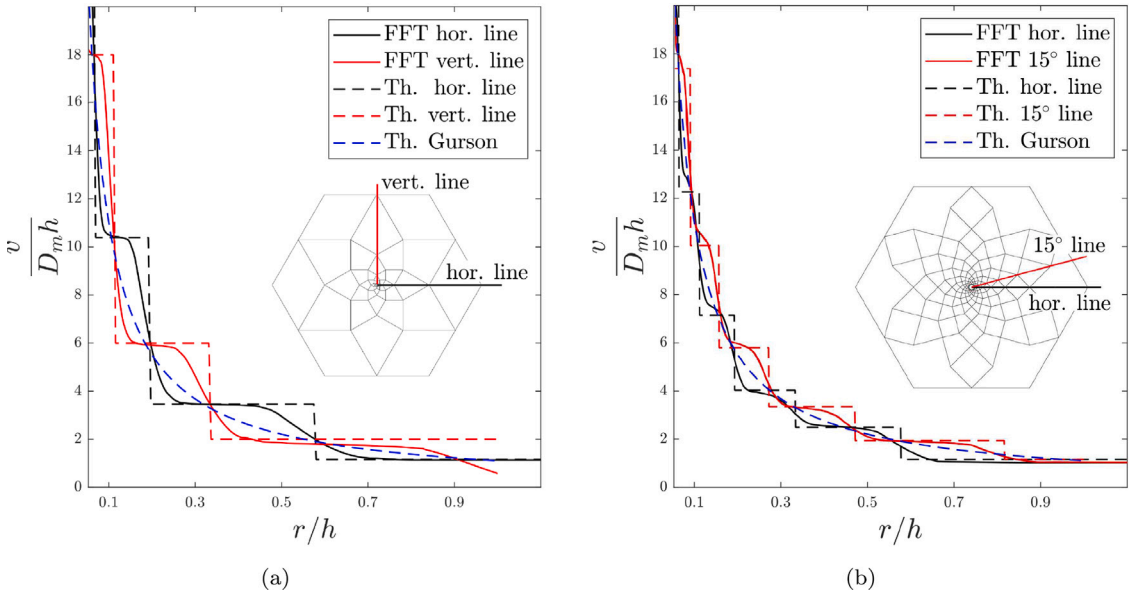

Fig. 16. Velocity along lines of the hexagonal cells with $f = 0.24\%$. (a) H0 cell and (b) H15 cell.

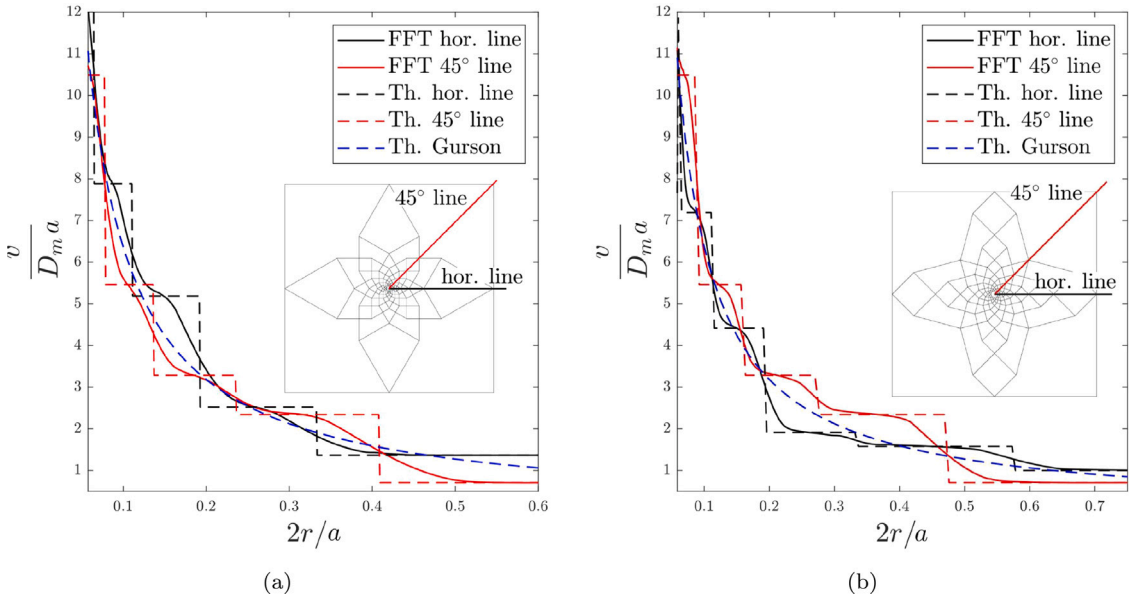

Fig. 17. Velocity along lines of the square cells with $f = 0.24\%$. (a) S0 cell and (b) S15 cell.

4. Macroscopic yield criteria of porous single crystals based on fractal velocity fields

4.1. Limit analysis framework

Limit-analysis, combined with the Hill–Mandel homogenization theory, is a powerful framework to derive constitutive equations for ductile porous solids. Indeed, it permits to perform efficiently the scale transition and thus to obtain a macroscopic plastic potential that depends on the underlying microstructure.

Let us consider a representative cell of a porous ductile solid denoted Ω containing a void denoted ω, and subjected to conditions of homogeneous boundary strain rate. The macroscopic yield locus of the porous material can be determined using the upper-bound theorem of limit-analysis (see e.g. Leblond et al., 2018). The fundamental inequality of this approach

$$\boldsymbol{\Sigma} : \mathbf{D} \leq \Pi(\mathbf{D}) \tag{27}$$

leads to the parametric equation of the yield locus

$$\boldsymbol{\Sigma} = \frac{\partial \Pi}{\partial \mathbf{D}}(\mathbf{D}). \tag{28}$$

The quantities $\boldsymbol{\Sigma}$ and $\mathbf{D}$ are respectively the macroscopic stress and macroscopic strain rate, defined as the volume averages of their microscopic counterparts $\boldsymbol{\sigma}$ and $\mathbf{d}$:

$$\boldsymbol{\Sigma} = \langle \boldsymbol{\sigma} \rangle_{\Omega}, \quad \mathbf{D} = \langle \mathbf{d} \rangle_{\Omega}, \tag{29}$$

where $\langle \cdot \rangle_{\Omega}$ denotes the spatial average over the representative cell Ω defined by Eq. (5). In Eqs. (27) and (28), the macroscopic plastic dissipation Π is defined as

$$\Pi(\mathbf{D}) = \inf_{v \in \mathcal{K}(\mathbf{D})} \langle \sup_{\boldsymbol{\sigma}^* \in C} \boldsymbol{\sigma}^* : \mathbf{d} \rangle_{\Omega}, \tag{30}$$

where C is the microscopic convex domain of reversibility and the set $\mathcal{K}(\mathbf{D})$ consists of the velocity fields $\boldsymbol{v}$ kinematically admissible with $\mathbf{D}$ and verifying the property of incompressibility.

Admissible velocity fields can exhibit tangential discontinuities across an interface S. In this case the plastic dissipation given by Eq. (30) is taken in the sense of distributions. The contribution of the surface term to the macroscopic dissipation then reads

$$\frac{1}{\mathrm{vol}(\Omega)} \int_S \sup_{\sigma^* \in C} \left(\boldsymbol{\sigma}^* . \boldsymbol{n}\right)_i \, [\![v_i]\!] \, \mathrm{d}S \tag{31}$$

where $[\![\boldsymbol{v}]\!]$ is the velocity jump across the interface S and $\boldsymbol{\sigma}^* . \boldsymbol{n}$ the traction acting on it, $\boldsymbol{n}$ being the interface normal.

In the case of a slip line having a tangential velocity jump $[\![\boldsymbol{v}]\!] = \dot{\Gamma} \boldsymbol{m}$, as defined in Section 3.1, the macroscopic surface dissipation (31) simply reduces to

$$\frac{l}{S_{\mathrm{cell}}} \times \dot{\Gamma} \tau_c, \tag{32}$$

where l is the length of the slip line and S_{cell} is the surface of the unit-cell ($S_{\mathrm{cell}} = a^2$ for square cells and $S_{\mathrm{cell}} = 2\sqrt{3}h^2$ for hexagonal cells).

4.2. Derivation of the yield limit

Due to the piecewise nature of the velocity field derived in Section 3, the strain rate is null in the blocks and all the strain energy is localized in the discontinuity of the velocity field, i.e in the slip lines. Then, using Eqs. (31) and (32), the macroscopic dissipation potential reads

$$\Pi(\mathbf{D}) = \frac{1}{S_{\mathrm{cell}}} \sum_{\text{slip line } \alpha} l_\alpha \dot{\Gamma}_\alpha \tau_c \tag{33}$$

where l_α and $\dot{\Gamma}_\alpha$ are respectively the length and the slip line velocity of the slip line α. Hereafter, the macroscopic yield limit is derived in the case of the H0 cell; the associated developments for the H15, S0 and S15 cells are given in Appendices A.1–A.3, respectively.

In order to calculate the macroscopic plastic dissipation (33), we must determine the length l_i of the slip lines in each layer i. Furthermore, since the slip line network proposed in Section 2 is fractal by definition, only the slip lines outside the void are relevant in the calculation of the plastic dissipation. Let us denote by $n(f)$ the number of layers outside the void. For the last layer outside the void (i.e. layer $n(f)$), the slip line is truncated (since it is partially in the void) and its length thus depends on the porosity. For the H0 cell, geometrical considerations give

$$n(f) = \left\lceil -\frac{\log\left(\frac{2\sqrt{3}}{\pi} f\right)}{2\log(3)} \right\rceil + \left\lfloor -\frac{\log\left(\frac{2\sqrt{3}}{\pi} f\right)}{2\log(3)} \right\rfloor, \tag{34}$$

$$l_i = h\left(\frac{\sqrt{3}}{3}\right)^{i+1}, \forall i < n(f) \quad ; \quad l_{n(f)} = h\left(\frac{3^{\frac{1-n(f)}{2}}}{2} - \sqrt{\frac{2\sqrt{3}}{\pi} f - \frac{3^{-n(f)}}{4}}\right). \tag{35}$$

Using Eqs. (26) and (33), the analytic expression of the macroscopic dissipation potential is given by:

$$\Pi(\mathbf{D}) = 4 D_m \tau^c \sum_{i=0}^{n(f)} \sqrt{3}^i \frac{l_i}{h}. \tag{36}$$

Since l_i/h only depends on f, the macroscopic plastic dissipation is a function of D_m and f. Finally, the yield limit is given by

$$\Sigma_m = \frac{1}{2} \frac{\partial \Pi}{\partial D_m} = 2\tau^c \sum_{i=0}^{n(f)} \sqrt{3}^i \frac{l_i}{h}. \tag{37}$$

4.3. Comparison of analytical and numerical macroscopic yield limit

The theoretical and numerical macroscopic yield limits are compared in Fig. 18 for the four cells considered (H0, H15, S0 and S15) and for several values of the porosity. In addition, the macroscopic yield limit obtained using the isotropic velocity field of Gurson (1977) for cylindrical cavities, following the method of Paux et al. (2015) in the case of spherical voids, is also represented in Fig. 18.

Overall, the theoretical predictions and the numerical results are in very good agreement and follow the same trends. A significant difference between the macroscopic yield limits of the hexagonal and square cells is observed, which is well captured by the theoretical model. This difference can be explained by the fact that the intervoid distance is smaller in the case of a square cell (for a given porosity), which implies that slip line network connecting the voids is smaller. Besides, the effect of crystalline orientation ($\theta = 0°$ or $\theta = 15°$), which appears to have a minor influence on the yield stress, is also reproduced by the model.

The predictions obtained using an isotropic velocity field (obtained for a cylindrical cell) significantly overestimate the yield stresses predicted numerically. These discrepancies have already been observed by Paux et al. (2015) in the case of spherical voids and are mainly due to the inaccurate description of the velocity field but also to the cell shape (which can be corrected using the heuristic Tvergaard (1981) parameter).

It should be noted that the upper-bound character of the theoretical criterion seems not to be preserved in some cases. In fact, this is due to (small) numerical errors induced by the difficulty to numerically reproduce discontinuous fields.

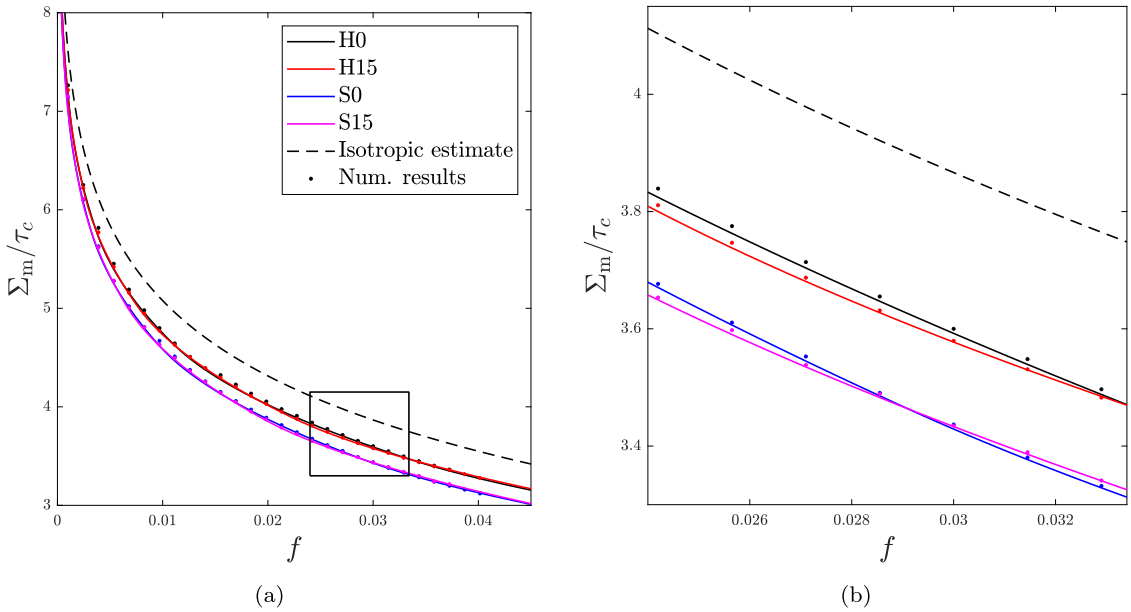

Fig. 18. Macroscopic yield limit of porous single crystals. (a) Global view and (b) Enlarged view.

5. Discussion

For the problem addressed, the proposed method has shown remarkable ability to predict the velocity field (Section 3.3) as well as the macroscopic yield criterion of the porous single crystal (Section 4.2). Here, we discuss firstly the influence of the boundary conditions on the velocity fields by considering the case of a cylindrical void in an infinite medium, already considered by Gan and Kysar (2007), and a randomly distributed population of voids, and secondly, the influence of the loading on the slip line network.

5.1. Cylindrical void in an infinite medium

The case of a cylindrical void in an infinite medium is considered here by comparison with the work of Gan and Kysar (2007). They derived the stress field by solving analytically the equilibrium equation $\operatorname{div} \boldsymbol{\sigma} = 0$ using the so-called slip line theory (Hencky, 1923; Prandtl, 1923). While giving the analytic solution for the stress field, the used method cannot provide the velocity field.

The obtained stress field is partitioned into stress sectors recalled in Fig. 19, each belonging to one slip system. The pattern induced by the stress sector is very similar to the fractal patterns of the velocity fields given in Figs. 9 and 10. Those velocity fields can be easily adapted so that the slip lines exactly match the boundaries of the stress sectors. Then, the velocity fields are compatible with the stress fields (i.e. every slip line lies on the corresponding stress sector) and are analytic solutions of the problem of the cylindrical void in an infinite medium. Our study thus complements the analytical solution of Gan and Kysar (2007) and paves the way to consider complex features such as the evolution of the shape of the cavities, the localization of the strain and the induced localization of the strain hardening.

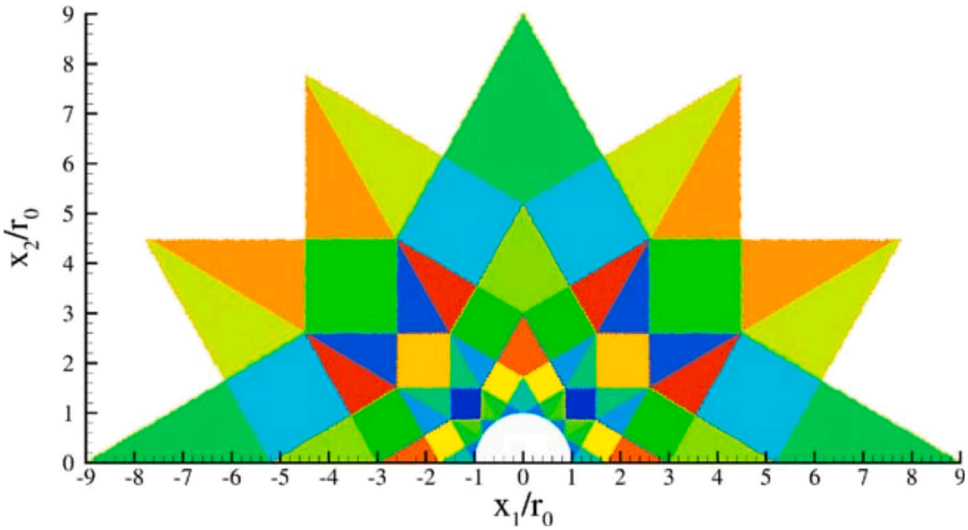

Fig. 19. Analytic stress sectors. Figure from Gan and Kysar (2007).

5.2. *Randomly distributed voids*

To further assess the influence of the boundary conditions, we have performed simulations with ten randomly distributed voids. Typical results are given in Fig. 20. As for the computations performed in Section 2.3, the strain is mainly concentrated in slip lines and forms complex slip line networks.

Around the cavities, one can observe fractal structures similar to those presented in Figs. 9 and 10, but missing some of the slip lines. Looking closely to the cavities in Fig. 20(b), it appears that the number of slip lines increases from layer to layer, and tends to have the twenty-four slip lines of the constitutive pattern given in blue in Fig. 10(a). Thus, for very low porosity, the velocity field around the cavities of a random distribution of voids is closed to the velocity fields obtained with the square cells and the H15 cell. This is consistent with the classical assumption made in the framework of the micromechanic study of ductile fracture: for low porosity, the distribution of the voids has little influence on the macroscopic behavior and on the growth of the cavities.

On the contrary, the velocity field around the cavities of a random distribution will significantly differ from the velocity field of the H0 cell, even for low porosity. Indeed, compared to the three other cells, the H0 cell has a peculiar fractal pattern (see Fig. 9(a)), leading to a peculiar velocity field around the void. This specificity comes from the alignment between the symmetry of the void

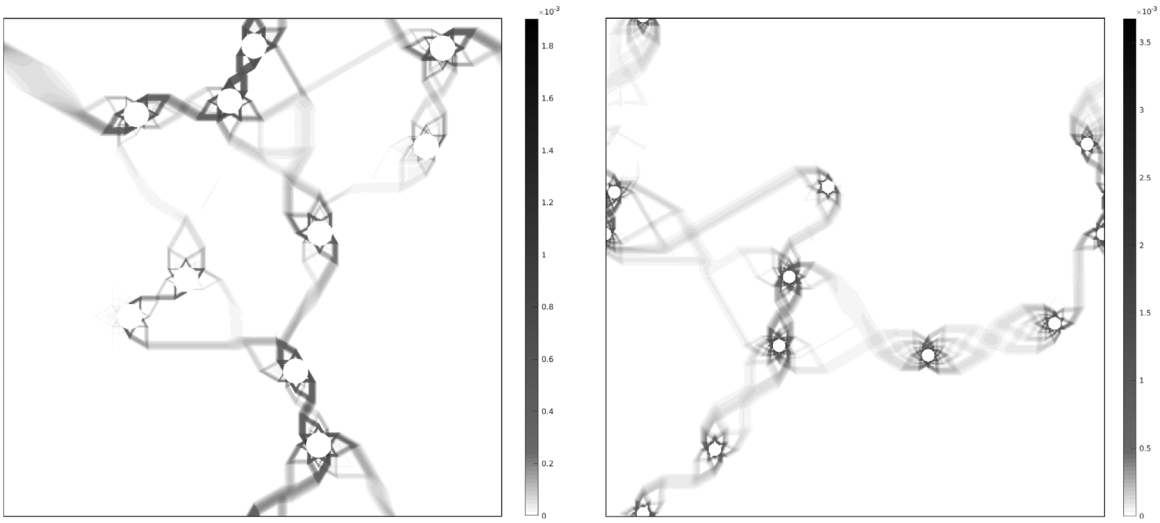

(a) (b)

Fig. 20. Equivalent von Mises strain for two configurations of ten randomly distributed voids with (a) $f = 2\%$ and (b) $f = 1\%$.

distribution and the crystalline orientation (0°, see Fig. 2(a)). Such symmetry never occurs in a random distribution of voids, thus, the H0 cell velocity field is not appropriate for such void distributions. As a general extension of this observation, one should avoid oversymmetrical situations to estimate the velocity field around the voids in porous crystalline material.

5.3. Influence of the loading on the slip line network

To consider other loadings, one needs to know the associated slip line networks. The influence of the loading on the slip line network is investigated for the H0 cell and a given porosity $f = 1.4\%$ by looking at the slip line network for different axisymmetric loadings with different strain triaxialities $T = E_m/E_{eq}$, with E_{eq} the von Mises equivalent strain. Two typical slip line networks are observed:

- At high triaxiality, slip line networks based on the fractal structure described in Fig. 9(a), but with different adaptative external layer as illustrated in Fig. 21(b).
- At zero triaxiality, slip line networks mainly constituted of four slip lines as illustrated in Fig. 21(a).

These observations suggest that, for a given microstructure and a given crystalline structure, the slip line networks are essentially stable. A given fractal structure can be applied to a wide range of loadings by modifying its slip line velocities. The determination of the slip line networks required to build a yield criterion can thus be reduced at a few deformation patterns which cover all the loadings. This extension of the proposed method will be the object of a future work.

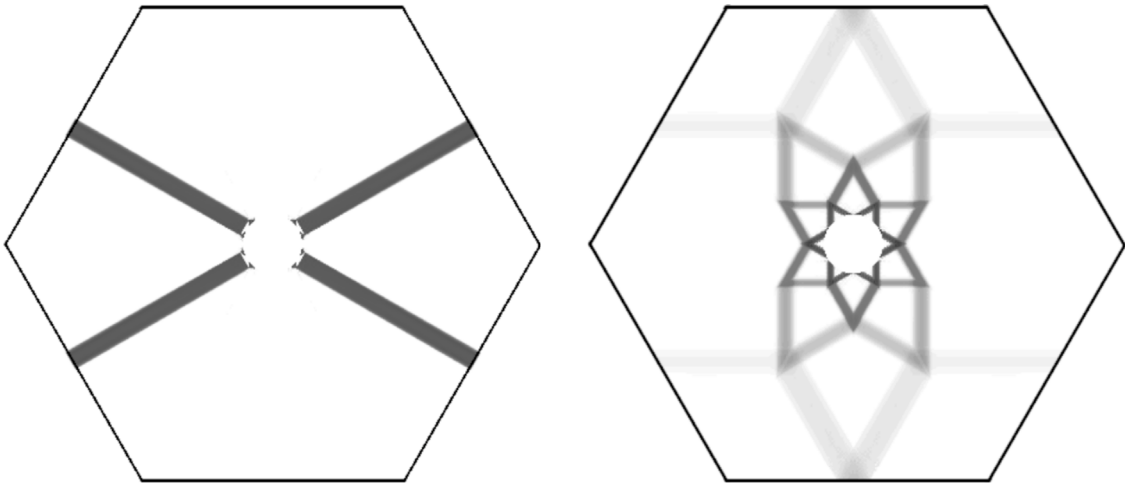

(a) (b)

Fig. 21. Equivalent von Mises strain for the H0 cell with porosity $f = 1.4\%$ and respective triaxialities (a) $T = 0$ and (b) $T = 2.5$.

6. Conclusions and perspectives

This work contributes to understand and model the influence of the plastic anisotropy on the velocity and strain fields in porous single crystals.

Numerical simulations using the fast-Fourier transform method have been performed to make an extensive study of the strain fields in hexagonal close-packed porous single crystals with cylindrical cavities. The strain fields appear to be mainly constituted of slip line networks. A closed observation of these networks unearths a fractal structure based on a constitutive pattern, common for cells or infinite medium with one cavity as well as for cells with a randomly distributed population of cavities. For cells with one cavity, we performed a geometrical reconstruction of the observed slip line fractal networks.

Assuming the strain field is solely made of these slip line networks, a general method to derive the associated velocity fields has been proposed and successfully applied to the different considered cells with one cavity. The velocity fields pave the way to *a priori* estimate of the evolution of the shape of the cavities. In particular, it should be used to predict the polyhedral shape of the cavities under high triaxiality observed numerically (Yerra et al., 2010; Srivastava and Needleman, 2013, 2015; Selvarajou et al., 2019) and experimentally (Crépin et al., 1996; Hong et al., 2017; Barrioz et al., 2019).

Furthermore, this model provides a single crystal based prediction of the localization of the strain, which could be used to predict the induced microscopic strain hardening. So far, it has been done by assuming homogeneous hardening (Ling et al., 2016) or under isotropic estimate of the strain localization (Paux et al., 2018). Nevertheless, the localization of the strain into slip bands is expected to strengthen the macroscopic hardening: locally, the hardening in the slip bands is more important than the hardening induced by homogeneously or isotropically distributed strain. With the proposed velocity field, it is possible to characterize much more precisely the localization of the strain, then the induced local hardening and, finally, the induced macroscopic hardening. It must be noted

that this process depends on the type of hardening law of the material and would require a thorough investigation to characterize its influence on the slip line patterns.

The obtained velocity fields have been used to derive the macroscopic yield criterion of the porous single crystal by kinematic limit-analysis. The assessment with the numerical results shows remarkable agreement, as it reproduces complex dependency such as the influence of the distribution of the voids and the crystalline orientation in the different considered cells, while the classical model based on the isotropic velocity field of Gurson (1977) significantly overestimates the macroscopic stress. Moreover, this agreement is obtained without any fitting parameter, while such criterion classically rely on the use of the heuristic Tvergaard parameters.

Finally, the approach proposed in this paper opens up the derivation of homogenized macroscopic behavior laws of porous single crystal taking into consideration their specific microscopic velocity field and the induced microstructural evolution (void shape and hardening localization). It is an important step to understand accurately the influence of the single crystal plastic behavior law on the ductile failure of crystalline materials. Nevertheless, at this stage, the reconstruction method has only been deployed for cylindrical cavities and must be extended for more realistic microstructures such as porous single crystals with spherical cavities. The extension of the method from 2D to 3D slip line networks might be cumbersome, especially for the identification of the slip bands, and remains a major difficulty to overcome.

CRediT authorship contribution statement

Joseph Paux: Conception and design of study, Writing – original draft. **Léo Morin:** Conception and design of study, Writing – original draft. **Renald Brenner:** Conception and design of study, Writing – original draft.

Declaration of competing interest

The authors declare that they have no known competing financial interests or personal relationships that could have appeared to influence the work reported in this paper.

Acknowledgments

All authors approved the version of the manuscript to be published.

Appendix. Velocity fields determination

A.1. H15 cell

In this appendix, we derive the slip line velocities in the H15 cell. Conventions (slip line velocities and block names) are given in Fig. A.22. Due to the symmetries, the slip line velocities of the external layer (between blocks A_j and B_j) are equal. We note $\dot{\Gamma}_0$ their slip line velocity. For any of the internal layer $i > 0$, the slip lines can be classed in two groups 1 and 2 with unique slip line velocities denoted by $\dot{\Gamma}_i^1$ and $\dot{\Gamma}_i^2$, respectively. In the layer 1, the first group is displayed in blue (slip lines in contact with blocks A_j) and the second group is shown in red (slip lines in contact with blocks B_j) (see Fig. A.22). The first layer can be described in this framework with fictitious slip lines given by

$$\dot{\Gamma}_0^1 = 0 \quad ; \quad \dot{\Gamma}_0^2 = \dot{\Gamma}_0. \tag{A.1}$$

The symmetries of the cell give the velocities orientation in the blocks A_j and B_j. They read

$$\mathbf{v}_{A_j} = v_A \left(\cos \frac{j\pi}{3} \mathbf{e}_1 + \sin \frac{j\pi}{3} \mathbf{e}_2 \right), \tag{A.2}$$

$$\mathbf{v}_{B_j} = v_B \left(\cos \left[\frac{\pi}{6} + \frac{j\pi}{3} \right] \mathbf{e}_1 + \sin \left[\frac{\pi}{6} + \frac{j\pi}{3} \right] \mathbf{e}_2 \right). \tag{A.3}$$

Introducing (A.2) and (A.3) in (20) as in Section 3.2, one obtains

$$v_A = \frac{2\sqrt{3}}{3} D_m h. \tag{A.4}$$

Applying relation (6) for the slip line between block A_0 and block B_0,

$$(\mathbf{v}_{A_0} - \mathbf{v}_{B_0}).\mathbf{n} = 0, \tag{A.5}$$

leads to

$$v_B = \frac{3 + \sqrt{6}}{3} D_m h. \tag{A.6}$$

Finally, one deduces the slip line velocity $\dot{\Gamma}_0$ through the slip line condition (7) reading

$$\dot{\Gamma}_0 \mathbf{m} = \mathbf{v}_{A_0} - \mathbf{v}_{B_0}, \tag{A.7}$$

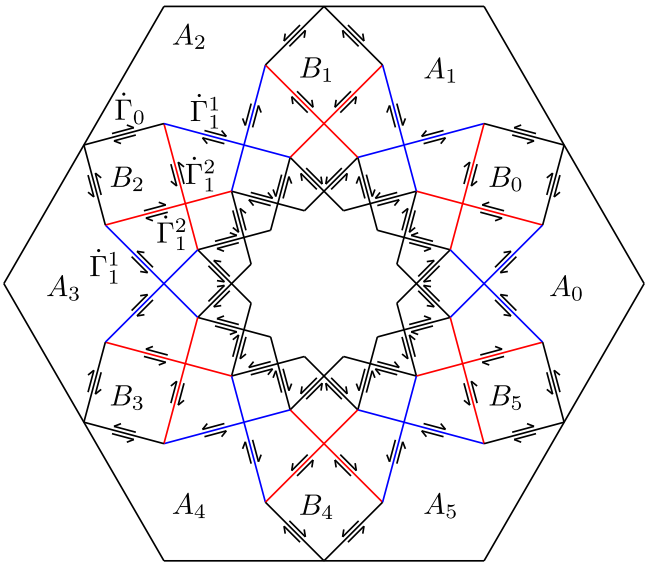

Fig. A.22. Conventions for the derivation of the H15 cell velocity field.

leading to

$$\dot{\Gamma}_0 = \frac{\sqrt{6}}{3} D_m h. \tag{A.8}$$

At this point, the boundary conditions led to the slip line velocities of the external layer of the fractal network. Then, we use the node condition (15) to determine recursively the slip line velocities of the internal layers:

$$\dot{\Gamma}_i^1 = \frac{\sqrt{3}}{3}\dot{\Gamma}_{i-1}^1 + \frac{2\sqrt{3}}{3}\dot{\Gamma}_{i-1}^2, \tag{A.9}$$

$$\dot{\Gamma}_i^2 = \frac{2\sqrt{3}}{3}\dot{\Gamma}_{i-1}^1 + \frac{\sqrt{3}}{3}\dot{\Gamma}_{i-1}^2. \tag{A.10}$$

To derive the yield limit as in Section 4.2, one also needs the expression of the slip line lengths in function of the porosity. Using the notations of Section 4.2, we obtain

$$n(f) = \left\lfloor \frac{\log\left(\frac{2\sqrt{3}f}{\pi}\right) - 2\log\left(\frac{\sqrt{6}}{3}\right)}{2\log\left(\frac{\sqrt{3}}{3}\right)} \right\rfloor, \tag{A.11}$$

$$l_0 = \frac{3\sqrt{2}-\sqrt{6}}{6}h \quad ; \quad l_1 = \frac{\sqrt{2}}{3}h \quad ; \quad l_{i+1} = \frac{\sqrt{3}}{3}l_i,\ \forall i > 1, \tag{A.12}$$

$$l_{n(f)} = \left(\frac{\sqrt{2}}{2}\left(\frac{\sqrt{3}}{3}\right)^{n(f)+1} - \sqrt{\frac{2\sqrt{3}f}{\pi} - \frac{1}{2}\frac{1}{3^{n(f)+2}}}\right)h. \tag{A.13}$$

Then, the yield limit for the square cell is determined by introducing the equations derived in this appendix in (33).

A.2. S0 cell

In this appendix, we derive the slip line velocities in the S0 cell. Conventions (slip line velocities and block names) are given in Fig. A.23. Due to the symmetries, the slip line velocities of the external layer (between blocks A_j and B_j) are equal. We note $\dot{\Gamma}_0$ their slip line velocity. For any of the internal layer $i > 0$, the slip lines can be classed in three groups with unique slip line velocities $\dot{\Gamma}_i^1$, $\dot{\Gamma}_i^2$ and $\dot{\Gamma}_i^3$, respectively. These groups are represented in Fig. A.23 by black slip lines, orange slip lines and blue slip lines, respectively for the first group, second group and third group. The first layer can be described in this framework with fictitious slip lines given by

$$\dot{\Gamma}_0^1 = 0 \quad ; \quad \dot{\Gamma}_0^2 = 0 \quad ; \quad \dot{\Gamma}_0^3 = \dot{\Gamma}_0. \tag{A.14}$$

In the same way, the second layer has fictitious third group slip lines $\dot{\Gamma}_1^3$=0.

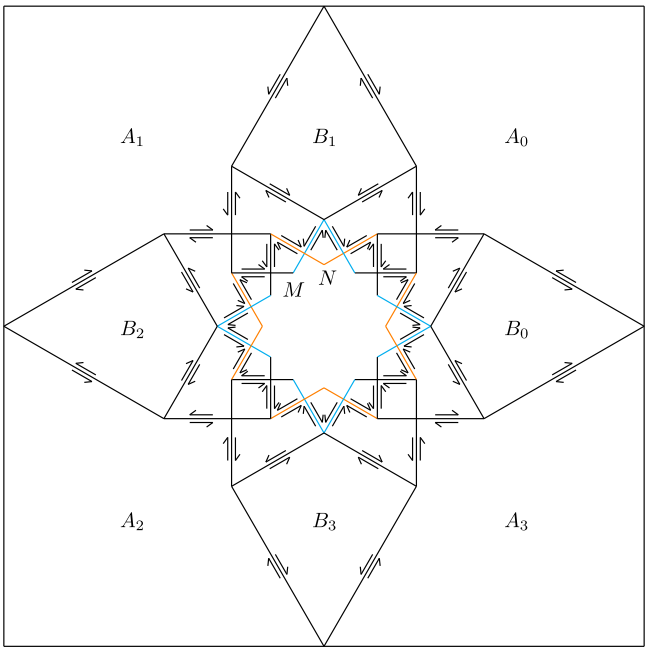

Fig. A.23. Conventions for the determination of the S0 cell velocity field.

The symmetries of the cell give the velocities orientation in the blocks A_j and B_j. They read

$$\mathbf{v}_{A_j} = v_A \left(\cos\left[\frac{\pi}{4} + \frac{j\pi}{2}\right] \mathbf{e}_1 + \sin\left[\frac{\pi}{4} + \frac{j\pi}{2}\right] \mathbf{e}_2 \right) \tag{A.15}$$

$$\mathbf{v}_{B_j} = v_B \left(\cos\frac{j\pi}{2} \mathbf{e}_1 + \sin\frac{j\pi}{2} \mathbf{e}_2 \right). \tag{A.16}$$

Introducing (A.15) and (A.16) in (20) as in Section 3.2, one obtains

$$v_A = \frac{\sqrt{2}}{2} D_m a. \tag{A.17}$$

Applying relation (6) for the slip line between block A_0 and block B_0,

$$(\mathbf{v}_{A_0} - \mathbf{v}_{B_0}).\mathbf{n} = 0, \tag{A.18}$$

one obtains

$$v_B = \frac{\sqrt{2} + \sqrt{6}}{2} v_A. \tag{A.19}$$

Finally, one deduces the slip line velocity $\dot{\Gamma}_0$ through the slip line condition (7) reading

$$\dot{\Gamma}_0 \mathbf{m} = \mathbf{v}_{A_0} - \mathbf{v}_{B_0}, \tag{A.20}$$

leading to

$$\dot{\Gamma}_0 = D_m a. \tag{A.21}$$

For any layer $i > 0$, one expresses the node condition at node M and N displayed in Fig. A.23 (N is a fictitious node for the transition between the first and the second layers). The node condition at N leads to

$$\dot{\Gamma}_i^3 = \sqrt{3} \dot{\Gamma}_{i-1}^2. \tag{A.22}$$

For the node M, it reads

$$\dot{\Gamma}_i^1 = \frac{\sqrt{3}}{3} \dot{\Gamma}_{i-1}^1 + \frac{2\sqrt{3}}{3} \dot{\Gamma}_{i-1}^3, \tag{A.23}$$

$$\dot{\Gamma}_i^2 = \frac{2\sqrt{3}}{3} \dot{\Gamma}_{i-1}^1 + \frac{\sqrt{3}}{3} \dot{\Gamma}_{i-1}^3. \tag{A.24}$$

To derive the yield limit as in Section 4.2, one also needs the expression of the slip line length in function of the porosity. Using the notation of Section 4.2, we obtain

$$n(f) = \left\lceil -\frac{\log\left(\frac{4f}{3\pi}\right)}{\log(3)} \right\rceil - 2 \tag{A.25}$$

$$l_0 = \frac{\sqrt{3}}{6}a \quad ; \quad l_{i+1} = \frac{\sqrt{3}}{3}l_i = \frac{1}{2}\left(\frac{\sqrt{3}}{3}\right)^{i+2} a, \qquad n(f) > i > 0 \tag{A.26}$$

$$l_{n(f)} = \left(\frac{3}{4}\left(\frac{\sqrt{3}}{3}\right)^{n(f)+2} - \sqrt{\frac{f}{\pi} - \frac{1}{16}\left(\frac{1}{3}\right)^{n(f)+1}}\right) a \tag{A.27}$$

Then, the yield limit for the square cell is determined by introducing the equations derived in this appendix in (33).

A.3. S15 cell

Finally, we derive in this appendix the slip line velocities in the S15 cell. Conventions (slip line velocities and block names) are given in Fig. A.24. Due to the symmetries, the slip line velocities of the external layer (between blocks A_j and B_j) are equal. We note $\dot{\Gamma}_0$ their slip line velocity. For any of the internal layer $i > 0$, the slip lines can be classed in three groups with unique slip line velocities $\dot{\Gamma}_i^1$, $\dot{\Gamma}_i^2$ and $\dot{\Gamma}_i^3$, respectively. These groups are represented in Fig. A.24 by black slip lines, orange slip lines and blue slip lines, respectively for the first group, second group and third group. The first layer can be described in this framework with fictitious slip lines given by

$$\dot{\Gamma}_0^1 = 0 \quad ; \quad \dot{\Gamma}_0^2 = 0 \quad ; \quad \dot{\Gamma}_0^3 = \dot{\Gamma}_0. \tag{A.28}$$

In the same way, the second layer has fictitious third group slip lines $\dot{\Gamma}_1^2$=0.

The symmetries of the cell give the velocities orientation in the blocks A_j and B_j. They read

$$\mathbf{v}_{A_j} = v_A\left(\cos\left[\frac{\pi}{4} + \frac{j\pi}{2}\right]\mathbf{e}_1 + \sin\left[\frac{\pi}{4} + \frac{j\pi}{2}\right]\mathbf{e}_2\right), \tag{A.29}$$

$$\mathbf{v}_{B_j} = v_B\left(\cos\frac{j\pi}{2}\mathbf{e}_1 + \sin\frac{j\pi}{2}\mathbf{e}_2\right). \tag{A.30}$$

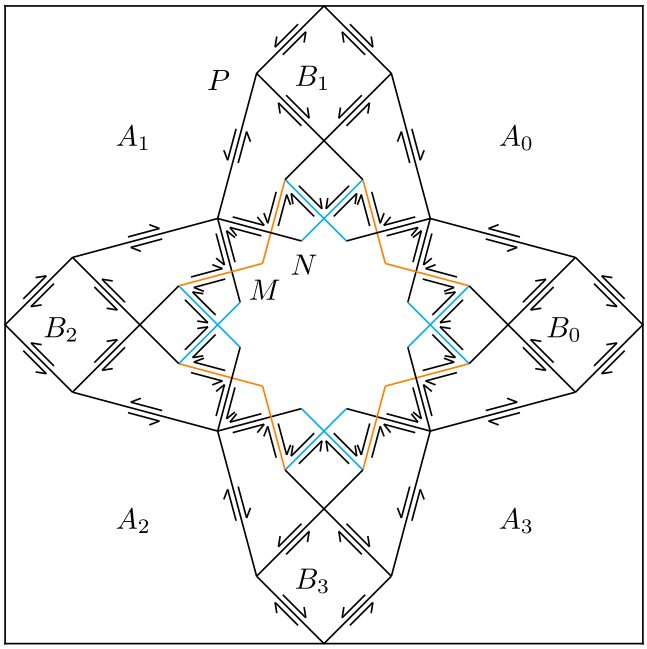

Fig. A.24. Conventions for the determination of the S15 cell velocity field.

Introducing (A.29) and (A.30) in (20) as in Section 3.2, one obtains

$$v_A = \frac{\sqrt{2}}{2} D_m a. \tag{A.31}$$

Applying relation (6) for the slip line between block A_0 and block B_0,

$$(\mathbf{v}_{A_0} - \mathbf{v}_{B_0}).\mathbf{n} = 0, \tag{A.32}$$

one obtains $v_B = D_m a$. Finally, one deduces the slip line velocity $\dot{\Gamma}_0$ through the slip line condition (7) reading

$$\dot{\Gamma}_0 \mathbf{m} = \mathbf{v}_{A_0} - \mathbf{v}_{B_0}, \tag{A.33}$$

leading to

$$\dot{\Gamma}_0 = \frac{\sqrt{2}}{2} D_m a. \tag{A.34}$$

For any layer i, one expresses the node condition at nodes M and N displayed in Fig. A.24. The node condition at M leads to

$$\dot{\Gamma}_i^1 = \sqrt{3}\, \dot{\Gamma}_{i-1}^2. \tag{A.35}$$

For the node N, it reads

$$\dot{\Gamma}_i^2 = \frac{\sqrt{3}}{3} \dot{\Gamma}_{i-1}^1 + \frac{2\sqrt{3}}{3} \dot{\Gamma}_{i-1}^3, \tag{A.36}$$

$$\dot{\Gamma}_i^3 = \frac{2\sqrt{3}}{3} \dot{\Gamma}_{i-1}^1 + \frac{\sqrt{3}}{3} \dot{\Gamma}_{i-1}^3. \tag{A.37}$$

To derive the yield limit as in Section 4.2, one also needs the expression of the slip line length in function of the porosity. Using the notation of Section 4.2, we obtain

$$n(f) = i \quad \text{such that} \quad r_{i+1} < a\sqrt{\frac{f}{\pi}} < r_i, \tag{A.38}$$

$$l_0 = \frac{3\sqrt{2} - \sqrt{6}}{12} a \quad ; \quad l_1 = \frac{\sqrt{2}}{6} a \quad ; \quad l_{i+1} = \frac{\sqrt{3}}{3} l_i, \forall i > 1, \tag{A.39}$$

$$l_{n(f)} = \left(\frac{\sqrt{2}}{4} - \sqrt{\frac{f}{\pi} - \frac{1}{8}} \right) a \quad \text{if} \quad n(f) = 0, \tag{A.40}$$

$$l_{n(f)} = \left(\frac{\sqrt{3}}{2} r_i - \sqrt{\frac{f}{\pi} - \frac{1}{4} r_i^2} \right) a \quad \text{if} \quad n(f) > 0. \tag{A.41}$$

where r_i is the radius of the porosity such that the void crosses the slip line network at the transition between layers i and $i+1$. r_i is obtained through

$$r_0 = \sqrt{\frac{3\sqrt{2} - \sqrt{6}}{12}}\, a \quad ; \quad r_i = \frac{2\sqrt{3}}{3} r_{i-1} - l_i \quad \forall i \geq 1. \tag{A.42}$$

Then, the yield limit for the square cell is determined by introducing the equations derived in this appendix in (33).

References

Agoras, M., Ponte Castañeda, P., 2013. Iterated linear comparison bounds for viscoplastic porous materials with "ellipsoidal" microstructures. J. Mech. Phys. Solids 61 (3), 701–725.

Barrioz, P.O., Hure, J., Tanguy, B., 2019. Effect of dislocation channeling on void growth to coalescence in FCC crystals. Mater. Sci. Eng. A 749, 255–270.

Benzerga, A.A., Besson, J., 2001. Plastic potentials for anisotropic porous solids. Eur. J. Mech. A Solids 20 (3), 397–434.

Borg, U., Kysar, J.W., 2007. Strain gradient crystal plasticity analysis of a single crystal containing a cylindrical void. Int. J. Solids Struct. 44 (20), 6382–6397.

Cheng, L., de Saxcé, G., Kondo, D., 2014. A stress-based variational model for ductile porous materials. Int. J. Plast. 55, 133–151.

Crépin, J., Bretheau, T., Caldemaison, D., 1996. Cavity growth and rupture of β-treated zirconium: A crystallographic model. Acta Mater. 44 (12), 4927–4935.

deBotton, G., Ponte Castañeda, P., 1995. Variational estimates for the creep behaviour of polycrystals. Proc. R. Soc. Lond. Ser. A: Math. Phys. Sci. 448 (1932), 121–142.

Gan, Y.X., Kysar, J.W., 2007. Cylindrical void in a rigid-ideally plastic single crystal III: Hexagonal close-packed crystal. Int. J. Plast. 23 (4), 592–619.

Gan, Y.X., Kysar, J.W., Morse, T.L., 2006. Cylindrical void in a rigid-ideally plastic single crystal II: Experiments and simulations. Int. J. Plast. 22 (1), 39–72.

Gologanu, M., Leblond, J.-B., Devaux, J., 1993. Approximate models for ductile metals containing non-spherical voids–Case of axisymmetric prolate ellipsoidal cavities. J. Mech. Phys. Solids 41 (11), 1723–1754.

Gurson, A.L., 1977. Continuum theory of ductile rupture by void nucleation and growth: Part I–Yield criteria and flow rules for porous ductile media. ASME J. Eng. Mater. Technol. 99 (1), 2–15.

Han, X., Besson, J., Forest, S., Tanguy, B., Bugat, S., 2013. A yield function for single crystals containing voids. Int. J. Solids Struct. 50 (14–15), 2115–2131.

Hencky, H., 1923. Über einige statisch bestimmte Fälle des Gleichgewichts in plastischen Körpern. ZAMM-J. Appl. Math. Mech./Z. Angew. Math. Mech. 3 (4), 241–251.

Hong, C., Fæster, S., Hansen, N., Huang, X., Barabash, R.I., 2017. Non-spherical voids and lattice reorientation patterning in a shock-loaded Al single crystal. Acta Mater. 134, 16–30.

Idiart, M.I., Ponte Castañeda, P., 2007. Variational linear comparison bounds for nonlinear composites with anisotropic phases. II. Crystalline materials. Proc. R. Soc. A 463 (2080), 925–943.
Jossel, L., Vincent, P.-G., Gărăjeu, M., Idiart, M.I., 2018. Viscoplasticity of voided cubic crystals under hydrostatic loading. Int. J. Solids Struct. 147, 156–165.
Khavasad, P.H., Keralavarma, S.M., 2021. Effective yield criterion for a porous single crystal accounting for void size effects. Mech. Mater. 160, 103950.
Kysar, J.W., Gan, Y.X., Mendez-Arzuza, G., 2005. Cylindrical void in a rigid-ideally plastic single crystal. Part I: Anisotropic slip line theory solution for face-centered cubic crystals. Int. J. Plast. 21 (8), 1481–1520.
Leblond, J.-B., Gologanu, M., 2008. External estimate of the yield surface of an arbitrary ellipsoid containing a confocal void. C. R. Méc. 336 (11–12), 813–819.
Leblond, J.-B., Kondo, D., Morin, L., Remmal, A., 2018. Classical and sequential limit analysis revisited. C. R. Méc. 346 (4), 336–349.
Leblond, J., Perrin, G., Devaux, J., 1995. An improved Gurson-type model for hardenable ductile metals. Eur. J. Mech. A Solids 14 (4), 499–527.
Lee, B.J., Mear, M.E., 1992. Axisymmetric deformation of power-law solids containing a dilute concentration of aligned spheroidal voids. J. Mech. Phys. Solids 40 (8), 1805–1836.
Ling, C., Besson, J., Forest, S., Tanguy, B.t., Latourte, F., Bosso, E., 2016. An elastoviscoplastic model for porous single crystals at finite strains and its assessment based on unit cell simulations. Int. J. Plast. 84, 58–87.
Madou, K., Leblond, J.-B., 2012a. A Gurson-type criterion for porous ductile solids containing arbitrary ellipsoidal voids—I: Limit-analysis of some representative cell. J. Mech. Phys. Solids 60 (5), 1020–1036.
Madou, K., Leblond, J.-B., 2012b. A Gurson-type criterion for porous ductile solids containing arbitrary ellipsoidal voids—II: Determination of yield criterion parameters. J. Mech. Phys. Solids 60 (5), 1037–1058.
Mbiakop, A., Constantinescu, A., Danas, K., 2015a. An analytical model for porous single crystals with ellipsoidal voids. J. Mech. Phys. Solids 84, 436–467.
Mbiakop, A., Constantinescu, A., Danas, K., 2015b. A model for porous single crystals with cylindrical voids of elliptical cross-section. Int. J. Solids Struct. 64–65, 100–119.
Michel, J.C., Moulinec, H., Suquet, P., 2001. A computational scheme for linear and non-linear composites with arbitrary phase contrast. Internat. J. Numer. Methods Engrg. 52 (12), 139–160.
Monchiet, V., Charkaluk, E., Kondo, D., 2011. A micromechanics-based modification of the Gurson criterion by using Eshelby-like velocity fields. Eur. J. Mech. A Solids 30 (6), 940–949.
Morin, L., Madou, K., Leblond, J.-B., Kondo, D., 2014. A new technique for finite element limit-analysis of Hill materials, with an application to the assessment of criteria for anisotropic plastic porous solids. Internat. J. Engrg. Sci. 74, 65–79.
Morin, L., Michel, J.-C., Leblond, J.-B., 2017. A Gurson-type layer model for ductile porous solids with isotropic and kinematic hardening. Int. J. Solids Struct. 118 (Supplement C), 167–178.
Moulinec, H., Suquet, P., 1998. A numerical method for computing the overall response of nonlinear composites with complex microstructure. Comput. Methods Appl. Mech. Engrg. 157 (1–2), 69–94.
Paux, J., Brenner, R., Kondo, D., 2018. Plastic yield criterion and hardening of porous single crystals. Int. J. Solids Struct. 132–133, 80–95.
Paux, J., Morin, L., Brenner, R., Kondo, D., 2015. An approximate yield criterion for porous single crystals. Eur. J. Mech. A Solids 51, 1–10.
Ponte Castañeda, P., 1991. The effective mechanical properties of nonlinear isotropic composites. J. Mech. Phys. Solids 39 (1), 45–71.
Prandtl, L., 1923. Anwendungsbeispiele zu einem henckyschen Satz über das plastische Gleichgewicht. ZAMM-J. Appl. Math. Mech./Z. Angew. Math. Mech. 3 (6), 401–406.
Rice, J.R., Tracey, D.M., 1969. On the ductile enlargement of voids in triaxial stress fields. J. Mech. Phys. Solids 17 (3), 201–217.
Selvarajou, B., Joshi, S.P., Benzerga, A.A., 2019. Void growth and coalescence in hexagonal close packed crystals. J. Mech. Phys. Solids 125, 198–224.
Song, D., Ponte Castañeda, P., 2017. A finite-strain homogenization model for viscoplastic porous single crystals: I – theory. J. Mech. Phys. Solids 107, 560–579.
Srivastava, A., Needleman, A., 2013. Void growth versus void collapse in a creeping single crystal. J. Mech. Phys. Solids 61 (5), 1169–1184.
Srivastava, A., Needleman, A., 2015. Effect of crystal orientation on porosity evolution in a creeping single crystal. Mech. Mater. 90, 10–29.
Subrahmanya Prasad, N., Narasimhan, R., Suwas, S., 2016. Numerical simulations of cylindrical void growth in Mg single crystals. Int. J. Fract. 200 (1), 159–183.
Tvergaard, V., 1981. Influence of voids on shear band instabilities under plane strain conditions. Int. J. Fract. 17, 389–407.
Yerra, S.K., Tekoglu, C., Scheyvaerts, F., Delannay, L., Van Houtte, P., Pardoen, T., 2010. Void growth and coalescence in single crystals. Int. J. Solids Struct. 47 (7–8), 1016–1029.